

RESEARCH ARTICLE

Cross-valley vortices in the Inn valley, Austria: Structure, evolution and governing force imbalances

Nevio Babić¹  | Bianca Adler²  | Alexander Gohm³  | Norbert Kalthoff¹  |
Maren Haid³  | Manuela Lehner³  | Paul Ladstätter³ | Mathias W. Rotach³ 

¹Institute for Meteorology and Climate Research, Karlsruhe Institute of Technology, Germany

²CIRES, University of Colorado Boulder, and NOAA/Physical Sciences Laboratory, Boulder, Colorado, USA

³Department of Atmospheric and Cryospheric Sciences, University of Innsbruck, Innsbruck, Austria

Correspondence

N. Babić, Institute for Meteorology and Climate Research, Karlsruhe Institute of Technology, Hermann-von-Helmholtzplatz 1, 76344 Eggenstein-Leopoldshafen, Germany.
Email: nevio.babic@kit.edu

Funding information

Deutsche Forschungsgemeinschaft (DFG), Grant/Award Number: 406279610; Karlsruhe Institute of Technology (KIT); the Austrian Science Fund (FWF); the Weiss Science Foundation, Grant/Award Number: P29746-N32

Abstract

Exchange of momentum and scalars in the mountain boundary layer is achieved through an interaction of meso-to-microscale motions, occurring to varying extents depending on the combined effect of thermally driven as well as dynamically driven forcings. One such motion, known as a secondary circulation, results from a horizontal force imbalance across a curved valley segment, wherein the centrifugal force towards the outside of the valley bend can create a pressure gradient force in the opposite direction. The lack of adequate measurement strategies capable of sampling such motions in curved mountain valleys explains the near-absence of any observational evidence of secondary circulations there. The goal of the CROSSINN (Cross-valley flow in the Inn valley investigated by dual-Doppler lidar measurements) campaign, conducted in a curved segment of the Inn valley, Austria, was to determine the character of the cross-valley flow by means of a coplanar retrieval applied to a multi-Doppler wind lidar configuration. A signature of a secondary circulation, hereafter referred to as a cross-valley vortex, stood out particularly during intense daytime upvalley flow episodes. Vortices were detected on 23 upvalley wind days, with a declining frequency of occurrence from August to October. Nearly all identified vortices were marked by a low-level upvalley jet, a clockwise wind direction turning with height, and a cessation of upvalley flow at the local ridgeline level. The routinely sampled coplanar-retrieved cross-valley wind field enabled the quantification of more advanced parameters based on vorticity, revealing a faster spin rate of the vortex around its streamwise axis given a stronger upvalley flow, and a period of revolution on the order of several tens of minutes. A detailed inspection of the lateral momentum budget and associated uncertainties confirmed the importance of the relationship between the centrifugal and the pressure gradient force for the cross-valley vortex occurrence in a curved valley.

KEYWORDS

complex terrain, CROSSINN, coplanar retrieval, Doppler lidar, momentum budget, mountain boundary layer, secondary circulation, streamwise vorticity

1 | INTRODUCTION

Unlike horizontally homogeneous and flat terrain, where the turbulent exchange occurs primarily in the vertical, the character of this exchange over heterogeneous and complex mountainous terrain assumes unavoidable three-dimensionality (Whiteman, 2000; Rotach *et al.*, 2014; Serafin *et al.*, 2018). Knowledge of such turbulent three-dimensional exchange is crucial for a proper description and forecasting of mountain weather, or equivalently, the exchange processes taking place within the mountain boundary layer (MoBL). Following the definition of the atmospheric boundary layer (ABL; Stull, 1988), the MoBL is defined as the lowest part of the troposphere directly influenced by the mountainous terrain, while responding to surface and terrain forcings with time-scales on the order of one to several hours (Lehner and Rotach, 2018). As such, the MoBL entails various exchange pathways, ranging from thermally driven flows such as valley and slope winds (Zardi and Whiteman, 2013; Adler and Kalthoff, 2014; Rotach *et al.*, 2015), to dynamically driven flows, driven by transient external forcing (Jackson *et al.*, 2013; Vosper *et al.*, 2018). These flows may further be coupled with surface convection (Adler and Kalthoff, 2014), inherently promoting the study of the MoBL to a multiscale problem.

Of largest economical, practical, and societal importance, mountain valleys are more significant than any other mountain feature (De Wekker *et al.*, 2018; Giovannini *et al.*, 2020). While mountain valleys represent just one type of a channel indentation in terrain, other types of channels submerged under water also host a myriad of geophysical flow features. On the one hand, subaerial channels, including rivers, estuaries and tidal channels, and on the other hand, subaqueous canyons on the ocean floor, span a broad range of depth-to-width aspect ratios. As is well known in the case of submerged meandering channels, the flow undergoes an adaptation to an imbalance of forces driven by the meandering, known as a secondary circulation (Azpiroz-Zabala *et al.*, 2017). A secondary circulation manifests itself as a helical vortex extending downstream of a channel curvature. When considering the cross-channel, lateral momentum budget in curvilinear coordinates (Kalkwijk and Booij, 1986), such a vortex is initiated by the centrifugal force that leads to a flow superelevation towards the outside of the channel bend. This superelevation, defined as an elevated water table at the outer bank, and a depressed water table at the inner bank, of a curved channel segment, drives a lateral pressure gradient force back towards the inside of the channel bend (Corney *et al.*, 2006; Azpiroz-Zabala *et al.*, 2017). Nonetheless, in both subaqueous and subaerial channels, there are numerous reports of case-dependent

instances deviating from this idealized force imbalance (Giorgio Serchi *et al.*, 2011). Furthermore, secondary circulations are not only key in governing deposition of sediments and suspended material in subaerial channels (Geyer and MacCready, 2014), but also in shaping morphological features along subaqueous canyons (Janocko *et al.*, 2013; Peakall and Sumner, 2015). We emphasize that secondary circulations driven by meandering channels should not be confused with like-named secondary circulations driven by contrasts in surface heterogeneities commonly encountered in the convectively driven ABL over flat terrain (Raasch and Harbusch, 2001; Van Heerwaarden *et al.*, 2014), or with asymmetric thermally driven circulations in complex terrain (Gohm *et al.*, 2009). To keep the distinction from the secondary circulations encountered in other curved channels and those generated by land-use heterogeneities, we will hereafter refer to a secondary circulation in a curved valley as a cross-valley vortex (CVV).

To our knowledge, only a single observational dataset, analyzed by Weigel and Rotach (2004) (hereafter WR04) and modelled subsequently by Weigel *et al.* (2006), revealed a CVV in the atmosphere driven by an upvalley flow encountering a curvature in the Riviera valley in Switzerland during the Mesoscale Alpine Programme (MAP). Despite many valleys worldwide exhibiting meandering in the along-valley direction, to the knowledge of the authors no other observational evidence of CVVs exists. It is therefore unknown to what extent a CVV may govern the distribution of heat, pollutants and momentum at a valley curvature. Furthermore, it remains unknown if the force imbalance determined for the Riviera valley (WR04) holds for other curved valleys. The underlying reason for the literature discrepancy between subaerial and subaqueous channels on the one hand, and valleys on the other hand, lies in both the spatial sampling scale as well as greater ease of studying these geophysical fluid phenomena in a laboratory setting. Particularly in case of subaerial channels, or simply rivers, their narrow widths and shallow depths encourage both consistent and cost-efficient vertical profiling along multiple discrete transects, using vessel-mounted acoustic Doppler profiler technology (Nidzieko *et al.*, 2009; Becherer *et al.*, 2015). Mountain valleys, up to several orders of magnitude wider and deeper than rivers, do not lend themselves easily to sampling strategies in an analogous fashion. At the time of the MAP campaign (WR04), costly *in situ* measurements collected by research aircraft were the only viable way of obtaining cross-valley transects capable of capturing the kinematic aspects of secondary circulations with adequate spatio-temporal detail. Since then, continuous development and ever-growing capabilities of remote-sensing instrumentation have enabled unique insights into ABL

and MoBL characteristics (Emeis *et al.*, 2018; Stith *et al.*, 2018). Along with instrument development, a simultaneous proliferation in the number of methodological approaches has led to new perspectives of flow kinematic structure. One of the most commonly utilized of these approaches is the multi-Doppler lidar retrieval of the two-dimensional wind projection of a three-dimensional flow, covering large spatial extents with ever finer temporal resolutions (Newsom *et al.*, 2005; Stawiariski *et al.*, 2013; Haid *et al.*, 2020; Haid *et al.* Personal communication, 2021).

In recent years, the multi-Doppler methodology has yielded unique insights into MoBL flow evolution, not just in valleys but in other complex terrain settings. Since the initial development of this method was intended for dual-radar set-ups (Davies-Jones, 1979), it has seen a growing application in the case of dual-lidar set-ups in recent years. Beyond a single pair of remote-sensing systems used for the retrieval, redundancy can be achieved with as many systems as possible (Haid *et al.*, 2020; Haid *et al.* Personal communication, 2021). Henceforth we will refer to this method as the coplanar-retrieval methodology, thereby implying that multiple lidars scan along the same spatial plane, resulting in a retrieval of a 2D wind field on this common spatial plane. Despite the coplanar-retrieval methodology being applied previously to horizontal planes, for instance in the Neckar valley in the vicinity of Stuttgart during the Urban Climate Under Change experiment ([UC]²; Adler *et al.*, 2020) or above the city of Innsbruck during the Penetration and Interruption of Alpine Foehn experiment (PIANO; Haid *et al.*, 2020; Haid *et al.* Personal communication, 2021), it has more commonly been applied to vertical planes. In the Owens valley, site of the Terrain-induced Rotor Experiment (T-REX; Grubišić *et al.*, 2008), novel insights about the evolution of subrotor vortices were gained with two Doppler lidars (Hill *et al.*, 2010). The coupling between wind turbines and MoBL flows, such as mountain waves, was thoroughly investigated during the recent Perdigo experiment in a valley with near-parallel mountain ridges in central Portugal (Wildmann *et al.*, 2018; Fernando *et al.*, 2019). Following one of the temporally longest sampling records of cross-valley flow structure collected in the Elorz valley in northern Spain during the ALEX17 campaign (Santos *et al.*, 2020), further detailed characterization of multi-scale MoBL flows is envisaged. Even in a small meteor crater during the METCRAX-II campaign (Lehner *et al.*, 2016), the understanding of warm air intrusions and small-scale hydraulic jumps could not have been advanced without the utilization of coplanar-retrieval methodology (Whiteman *et al.*, 2018a, 2018b). In all of the above campaigns performing Range-Height Indicator (RHI) type scans, the preferential alignment of the Doppler lidar

scanning planes was along the climatologically prevalent flow direction, with flow usually impinging perpendicularly onto a mountain ridge (Hill *et al.*, 2010; Wildmann *et al.*, 2018) or a crater rim (Whiteman *et al.*, 2018a, 2018b). Conditions during which the main flow direction is mainly perpendicular to the scanning planes have received no attention to date, largely due to ambiguities when interpreting flow with attack angles not aligned with the scanning plane itself. However, it is exactly during such conditions, for instance during intense along-valley flow parallel to the valley sidewalls, when a CVV is most likely to develop in a curved valley channel (WR04). This omission of conditions with flow perpendicular to the scanning plane, together with the sampling scale disparity between valleys and submerged channels, explains the lack of necessary measurements capable of elucidating CVVs in valleys.

To advance the knowledge of cross-valley flow kinematic structure, we conducted the ‘Cross-valley flow in the Inn valley investigated by dual-Doppler lidar measurements’ (CROSSINN) campaign in the Inn valley, Austria, from 01 August to 13 October 2019 (Adler *et al.*, 2021d). The Inn valley is one of the most instrumented Alpine valleys with an observational sampling history spanning several decades and research efforts (e.g., Brehm and Freytag, 1982; Freytag, 1987; Gohm *et al.*, 2009, 2010; Harnisch *et al.*, 2009; Haid *et al.*, 2020; Haid *et al.* Personal communication, 2021; Karl *et al.*, 2020; Umek *et al.*, 2020). Furthermore, the Innsbruck Box (i-Box; Rotach *et al.*, 2017), a long-term eddy-covariance network situated in the vicinity of Innsbruck, continually advances the knowledge of MoBL processes (Massaro *et al.*, 2015; Stiperski and Rotach, 2016; Goger *et al.*, 2018, 2019; Sfyri *et al.*, 2018; Lehner *et al.*, 2019, 2021; Stiperski *et al.*, 2019). Preliminary analyses (Adler *et al.*, 2021d) revealed that CVV may have formed in the CROSSINN investigation area, with a resemblance to the secondary circulations found in subaerial and subaqueous channels. The CROSSINN dataset therefore represents an ideal opportunity to sample, for the first time, cross-valley flow using the coplanar-retrieval methodology, for the investigation of CVV mechanics. The long-term placement of the i-Box facilities in the middle of the CROSSINN investigation area further augments our observational dataset. The present study addresses the following three questions:

- (a) Under what atmospheric conditions do CVVs form at a valley bend?
- (b) To what extent does the magnitude of the along-valley flow determine the development of a CVV?
- (c) Does the force imbalance leading to a CVV in a valley correspond to the one for secondary circulations found in subaerial and subaqueous channels?

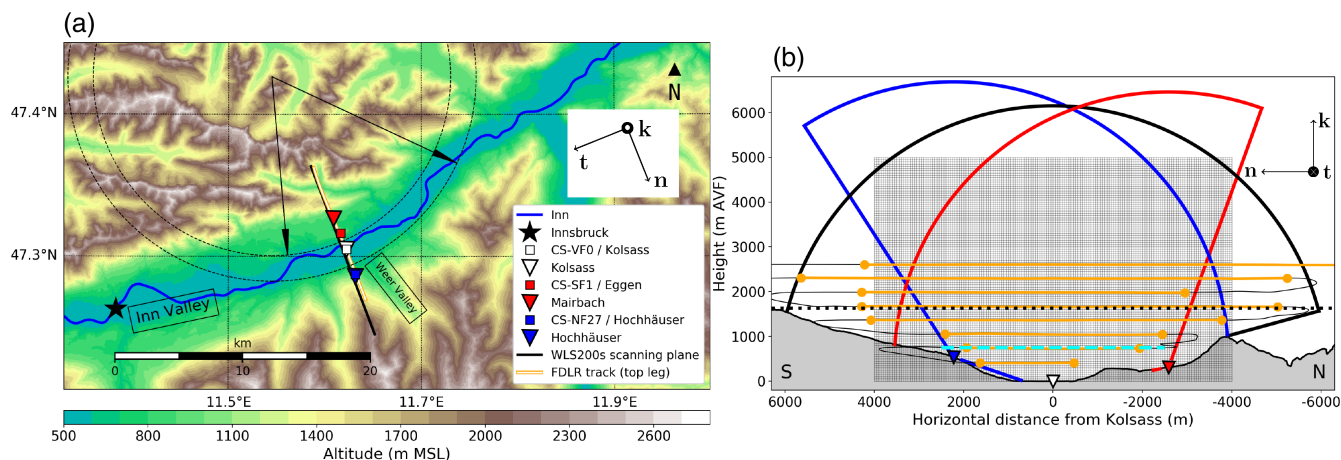


FIGURE 1 (a) Topographic representation of the lower Inn valley. The coloured squares indicate the locations of the i-Box flux towers analyzed in this study, with the labels denoting the official i-Box designation and the closest populated residential area. The coloured triangles indicate the locations of the three Windcubes. The black line represents the plane of the coplanar-retrieved wind field, while the white line with the orange border denotes the straight flight track segment of the topmost cross-valley leg flown during IOP4. The inner and outer dashed circles have radii of 14 and 16 km, respectively. The annotated boxes show the positions and orientations of the main Inn and tributary Weer valleys. The inset coordinate axes represent the natural coordinate system with an origin at Kolsass, with \mathbf{t} the streamwise unit vector aligned with the upvalley flow, \mathbf{n} the normal unit vector pointing to the left of the upvalley flow, and \mathbf{k} the vertical unit vector. (b) Cross-valley representation of the CROSSINN area of interest. The three coloured circular segments, each of radius 6,150 m, denote the extent of the RHI of each corresponding Windcube. The rectangular mesh represents the coplanar retrieval grid. The thin black lines denote the cross-valley flight tracks, while the orange lines denote the specific straight segments used for the analyses. The horizontal dotted black line indicates the altitude of the average ridgeline level equal to 1,630 m AVF, while the horizontal dashed cyan line indicates an altitude of 750 m AVF shown in Figure 2a. The letters N and S denote the northern and southern edges of the cross-section, respectively. Triangle markers and the inset coordinate system are the same as in (a) [Colour figure can be viewed at wileyonlinelibrary.com]

The study is organized as follows. Section 2 covers the aspects of the investigation area, instruments used, as well as the methodology deployed to obtain the coplanar-retrieved wind fields from which periods with CVVs are identified. Section 3 provides an overview of the conditions both inside and above the Inn valley at the time of CVV occurrence. In Section 4 we determine the relevance of upvalley flow in sustaining a CVV, while in Section 5 we determine the leading-order terms of the lateral momentum budget components and resulting force imbalances for two case-study periods with and without a CVV. Upon providing a discussion of several additional aspects in Section 6, we summarize the main findings of the study in Section 7.

2 | INVESTIGATION AREA, INSTRUMENTATION, DATA AND METHODS

2.1 | Site details

CROSSINN took place in the lower Inn valley, approximately 18 km northeast of the city of Innsbruck (Figure 1a). The valley in this region is approximately

20 km wide crest-to-crest, approximately 1,630 m deep (Adler *et al.*, 2021d), while the valley floor is flat in the cross-valley direction for roughly 2 km. The valley floor slopes slightly in the upvalley direction, towards southwest. It is dominated by a mixture of residential and cultivated areas, while the neighbouring valley sidewalls are mostly forested. The southern valley sidewall is characterized by a number of tributary valleys exiting nearly perpendicularly into the Inn valley. Although the northern sidewall possesses no similar tributaries, it is characterized by a relatively flat, nearly 2 km wide plateau, extending approximately 300 m above the valley floor (AVF; Figure 1b). The valley floor itself is located at an altitude of 546 m above mean sea level (amsl).

Common for the base of both valley sidewalls is their near-circular geometry across a 60° azimuthal sector (Figure 1a). In other words, the base of the northern sidewall tracks along a circle of radius 14 km, while the base of the southern sidewall tracks along one of radius 16 km. Therefore, for the sake of retaining simplicity in the lateral momentum budget examination, we will use a representative valley curvature $R = 15$ km. If the valley as a whole is considered, this slight curvature can rather be interpreted as an inflection in the valley profile. Finally, it is necessary to mention that the valley to the southwest

of this curvature is slightly narrower than to the northeast of it (e.g., Vergeiner and Dreiseitl, 1987, their figure 14; Zängl, 2004, his figures 3a and 9a). In turn, such a narrowing of the valley width may serve to amplify the daytime, northeasterly upvalley flow on its propagation through the valley bend.

2.2 | *In situ* instrumentation

2.2.1 | i-Box

The siting of CROSSINN instrumentation was primarily influenced by the locations of the long-term i-Box flux towers (Rotach *et al.*, 2017). Specifically, the three flux towers of interest for the present study were CS-VF0, CS-SF1, and CS-NF27, where CS stands for core site, VF for valley floor, NF and SF for north-facing and south-facing respectively, and the digit represents the local slope angle in degrees. For brevity, these sites will be denoted as Kolsass, Eggen, and Hochhäuser, respectively (Figure 1a).

Here we use measurements subjected to traditional eddy-covariance quality-control procedures as outlined in Stiperski and Rotach (2016) and Rotach *et al.* (2017). Kolsass, Eggen and Hochhäuser were equipped with sonic anemometers at heights of 8.7, 6.75 and 6.8 m above ground level (agl), respectively. In addition to wind information, here we also use scalar measurements of temperature, humidity, pressure, radiation and precipitation from Kolsass and Hochhäuser. The post-processed scalar and wind quantities, as well as integral turbulence statistics, are available for analysis at 1- and 30-min temporal resolutions, respectively. Finally, Kolsass also acted as the headquarter site for Intensive Observation Period (IOP) operations and for the housing of the majority of accompanying KITcube instrumentation (Kalthoff *et al.*, 2013).

2.2.2 | Radiosoundings

During a total of ten IOPs conducted during CROSSINN (Adler *et al.*, 2021d), routine radiosondes were launched at discrete times from Kolsass to provide highly resolved *in situ* measurements of base thermodynamic variables. Each IOP was envisaged as a full 24-hr cycle with a total of ten radiosonde launches, spaced 2 hr apart during daytime and 3 to 4 hr apart during night-time. IOPs were primarily targeted at sampling fair-weather, thermally driven conditions with weak synoptic disturbance. For a complete overview of each IOP and exact launch times, we refer the reader to Adler *et al.* (2021d), their figure 3. Each sounding consisted of a GRAW DFM-09 sonde, relaying GPS and atmospheric information via a radio transmitter to Kolsass.

The temporal resolution of the processed measurements was 2 s, yielding an average vertical resolution of 10 m in the lower troposphere.

2.2.3 | Aircraft measurements

In situ aircraft measurements were also conducted during five IOPs in August 2019. The D-FDLR Cessna Grand Caravan 208B (DLR) flew a total of four sets of cross-valley flights as well as four sets of along-valley flights during the selected IOPs (Adler *et al.*, 2021d). Of interest for the present study are the fourth cross-valley flights which took place during late afternoon of IOP 2b (9 August) and IOP 4 (14 August), consisting of eight vertically stacked legs which were aligned with the vertical scanning plane (black line in Figure 1a). These legs were flown in a back-and-forth pattern across the valley, with the lowest leg at approximately 400 m AVF and the highest leg at approximately 2,600 m AVF, yielding an average vertical separation of 300 m. Here we analyze the post-processed 10 Hz *in situ* measurements of wind and scalars, sampled by the METPOD sensor package (Mallaun *et al.*, 2015). In the remainder of the study, the aircraft measurements will be denoted as FDLR measurements.

2.3 | Remote-sensing instrumentation

Adler *et al.* (2021d), their Table 3, gives a detailed overview of technical characteristics, scan types, and scan configurations concerning the remote-sensing instrumentation. Here we focus on describing only a subset of the overall remote-sensing instrumentation of relevance for the present analysis.

2.3.1 | Windcube Doppler lidars

Three Windcube WLS-200s lidar systems, developed by Leosphere and constituting an integral component of the KITcube, were deployed at three different locations in the investigation area. Adler *et al.* (2021d), their figure 2, gives a depiction of the surroundings of each Windcube. The first Windcube was deployed at Kolsass with an unobstructed view from northwest towards southeast (Figure 1). The second Windcube was deployed approximately 100 m from the Hochhäuser flux tower, up the southern sidewall at 536 m AVF. This Windcube had a clear line of sight towards the northwest, while the terrain and forest upslope of the lidar prevented broader scanning towards southeast. Finally, the third Windcube was deployed in Mairbach next to a clearing looking towards southeast at an altitude 310 m AVF, approximately

1 km to the northwest of the Eggen flux tower. Similar to Hochhäuser, a treeline located immediately next to the lidar prevented it from scanning further towards the northwest. For consistency, we will refer to these three locations as Kolsass, Hochhäuser, and Mairbach, respectively. We note that Kolsass and Hochhäuser will be used interchangeably to refer to either the i-Box flux tower or their respective Windcube. Given their larger separation, we will keep the distinction between Mairbach and Eggen.

The accurate positioning of the three Windcube systems, in an area of extremely heterogeneous complex terrain, yielded three nearly perfectly aligned scanning planes (Figure 1a). Due to local terrain and land-use characteristics, the three planes were not perfectly aligned, with an approximately 120 m offset along the valley at the most. The only role of the three systems during CROSSINN was to perform RHI scans at an azimuth angle of 158.15° . In this manner, the RHI scans were perpendicular to the local along-valley axis with an azimuth of 68.15° . The outlines of all three RHI scans are demonstrated in Figure 1b, revealing a large area where the three scanning planes overlapped. Each RHI scan lasted 1 min, providing radial velocity v_r , carrier-to-noise ratio (CNR), and relative backscatter at a physical resolution of 100 m, with overlapping range gate distance of 50 m, and a temporal resolution of 0.25 s. Further details concerning the RHI scan parameters and post-processing criteria can be found in Adler *et al.* (2021d).

2.3.2 | Halo Doppler lidars

Due to the specific scanning strategy of the Windcubes, two additional Doppler lidars, part of the Innsbruck Atmospheric Observatory (IAO; Karl *et al.*, 2020) were deployed at Kolsass to provide auxiliary information on the vertical and horizontal structure of the flow. Therefore, the underlying purpose of the two additional lidars was to reduce the ambiguity concerning the attack angle of the upvalley flow onto the Windcube RHI planes, as well as to provide turbulence and horizontal wind information. Two Halo Photonics Stream Line lidars, denoted as SL88 and SLXR142 in the remainder of the study, were deployed in the near-vicinity of the Kolsass flux tower. The SL88, having a generally smaller range than the SLXR142, performed repeated full-circle plan position indicator (PPI) scans at an elevation angle of 70° at a temporal resolution of roughly 80 s. On the other hand, the SLXR142 performed a recurring pattern consisting, among others, of a single full-circle 70° elevation PPI at the 0 and 30 min mark of each hour.

The range gate distance for both SL88 and the SLXR142 equalled 36 m. Upon the application of the Velocity Azimuth Display (VAD; Browning and Wexler,

1968) algorithm to raw radial velocities of each 70° PPI scan for both lidars, vertical profiles of horizontal wind were obtained. To filter out potentially erroneous wind estimates, all range gates with a signal-to-noise ratio (SNR) less than -24 dB were omitted.

2.3.3 | Ceilometer

To provide vertical profiles of uncalibrated backscatter and evidence of potential layering above Kolsass, we deployed a CHM 15k backscatter ceilometer. Given that precipitation left a signature in the measurements via increased backscatter, the measurement output at 60 s temporal and 15 m vertical resolution were used to define a custom precipitation flag. The reason for this was the fact that the rain gauge measurements at Kolsass were often observed to miss light precipitation events (not shown). Additionally, we found that precipitation, not necessarily reaching Kolsass but also other locations in the investigation area, often left a signature in the coplanar-retrieved vertical velocity w as large negative values. Since such values indicate the fall velocity of hydrometeors rather than sinking motion, we resorted to defining a custom precipitation flag to discard such conditions. Specifically, we declared a particular 1 min interval as precipitation if the backscatter exceeded a threshold value of 55 dB in at least 20% of the vertical profile between 0 and 4,000 m AVF. It is important to emphasize that such a flag is sufficient to identify only potential precipitation occurrences above Kolsass, however large negative w above the valley sidewalls may still remain unfiltered.

2.4 | Supplemental datasets

To determine the large-scale conditions above the valley ridgeline during all 74 days of the CROSSINN field phase, we computed daily averages of horizontal wind speed and direction at the 700 hPa level from the hourly ERA5 reanalysis (Hersbach *et al.*, 2020). Specifically, for each day of the campaign, we computed a temporal average for the period between 1200 and 2000 UTC (local time = UTC+2 hr) for the grid point closest to Kolsass ($11^\circ 36'E$, $47^\circ 18'N$). This period was chosen as the most representative concerning the upvalley flow phase to be discussed.

To obtain information of pressure variability at the exit of the Inn valley, we resorted to the 10-min time series from a TAWES (TeilAutomatische WetterStationen) weather station located at Kufstein ($12^\circ 9' 46''E$, $47^\circ 34' 31''N$), maintained by the Austrian national weather service ZAMG. Although Kufstein is located at the exit of the Inn valley, approximately 50 km northeast of Kolsass, we assume it to be representative of the Bavarian foreland located further to the north. We note that we first reduced the pressure

at Kufstein to the respective height of Kolsass using the hypsometric equation (Holton, 2004), given that the elevation difference between the two stations is approximately 56 m.

2.5 | Methodology

2.5.1 | Natural coordinate system

Given the orientation of the Windcube RHI scans perpendicular to the along-valley axis, we adopt the natural coordinate system (Figure 1; Holton, 2004) when analyzing the Windcube RHI measurements and the FDLR measurements. In this frame of reference, the along-valley axis corresponds to the streamwise unit vector \mathbf{t} (positive south-westward), the normal unit vector \mathbf{n} (positive southeastward) is parallel to the Windcube RHI planes and pointing to the left of the northeasterly upvalley flow, and the vertical unit vector \mathbf{k} is equivalent to its Cartesian counterpart (positive upwards). Therefore, the wind speed components in this frame of reference correspond to the along-valley streamwise component u_s , the cross-valley normal component u_n , and the vertical component u_z . Therefore, the vertical component in this new frame of reference is equivalent to its Cartesian counterpart w . We point out that, in the case of all other datasets analyzed in this study, we retain the customary Cartesian frame of reference.

2.5.2 | Coplanar retrieval

The alignment of the three RHI scans from each Windcube, along with their synchronized durations, enabled the retrieval of a two-dimensional wind \mathbf{v}_v in their common vertical scanning plane, based on post-processed radial velocity measurements. On their own, radial velocity measurements represent the projection of a three-dimensional wind onto the laser beam (Banta *et al.*, 2013). When the azimuth is fixed, as in our case, the problem reduces to two dimensions, resulting in the following expression for radial velocity:

$$v_r = \hat{\mathbf{r}}_v \cdot \mathbf{v}_v, \quad (1)$$

where $\hat{\mathbf{r}}_v$ is the two-dimensional unit vector in the vertical RHI plane, and \mathbf{v}_v is the desired two-dimensional projection of the three-dimensional wind onto this plane. A number of previous studies have utilized two Doppler lidars to obtain \mathbf{v}_v (Calhoun *et al.*, 2006; Hill *et al.*, 2010; Cherukuru *et al.*, 2015; Whiteman *et al.*, 2018a; 2018b; Wildmann *et al.*, 2018). Similar to Adler *et al.* (2020) and Haid *et al.* (2020; Haid *et al.* Personal communication, 2021), here we had the advantage of a third lidar to expand the retrieval coverage. Note that, even though three lidars

are ultimately available, the retrieval is still yielding only two components of the 3D wind vector. We utilized the coplanar retrieval algorithm of Haid (2019), by retrieving \mathbf{v}_v onto a 8 km wide and 5 km tall Cartesian mesh with a lattice width $\Delta l = 50$ m (Figure 1b). At each grid point of the retrieval mesh, N total radial velocity estimates from all three Windcubes were collected inside of a radius of influence $R = \Delta l / \sqrt{2}$, yielding a system of N linear equations, solved here through a minimization of its cost function (Newsom *et al.*, 2005):

$$J = \sum_{i=1}^N (v_{r,i} - \hat{\mathbf{r}}_v \cdot \mathbf{v}_v)^2. \quad (2)$$

The retrieved \mathbf{v}_v was rejected if the intersection angle of the original Windcube beams was outside of the interval $[30^\circ, 150^\circ]$ simultaneously for all lidar pairs. Although this step in the retrieval discarded erroneous \mathbf{v}_v due to nearly co-linear beams, it did preclude the analysis of \mathbf{v}_v close to the valley sidewalls (Adler *et al.*, 2021d, their figure 4f). The wind components u_n and u_z that define the wind vector $|\mathbf{v}_v| = \sqrt{u_n^2 + u_z^2}$, represent respectively the cross-valley horizontal wind component and vertical wind component in the RHI scanning plane. During CROSSINN, the average horizontal extent of the retrieved wind field amounted to approximately 6 km with little change over time. The vertical extent varied more drastically, depending primarily on the aerosol and moisture loading above the ridgeline, as well as on dew formation on top of the Windcube scanner at Kolsass during clear nights when cold pools frequently formed above the valley floor. Above Kolsass the vertical extent of the retrieved wind field has a median value of 2,250 m AVF during the entire campaign, with an interquartile range of 1,500 m.

2.5.3 | Identification of CVV in the Inn valley

A CVV at any cross-section of a curved channel manifests itself through spatially coherent regions of upward and downward vertical motions, depending on channel geometry, channel curvature, as well as along-channel flow depth and strength (Russell and Vennell, 2014, their figure 8). To determine the presence or lack of such coherent regions in the CROSSINN investigation area, we focused on coplanar-retrieved u_z across the Inn valley, specifically a single cross-valley transect at 750 m AVF (Figure 1b). This transect, shown in Figure 2a, is above the region excluded by the intersection angle criterion, but is still within the valley atmosphere below the average ridgeline height. To reduce noise in the raw 1-min coplanar-retrieved u_z , we calculated 30-min u_z averages at each grid point of the retrieval mesh, omitting those grid points having less than 15 available 1-min u_z values. Gaps

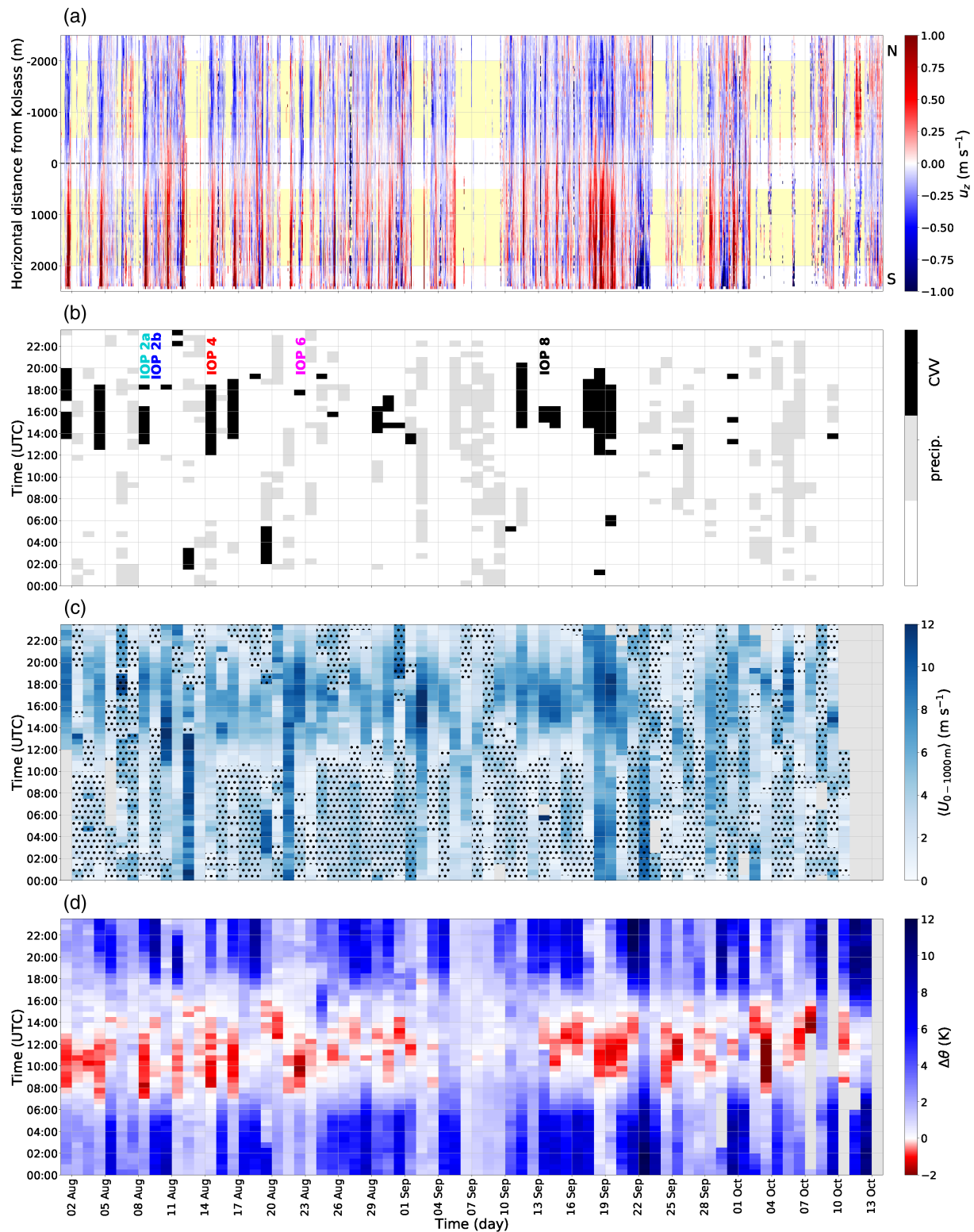


FIGURE 2 (a) Time–distance visualisation of the coplanar-retrieved vertical velocity component u_z at 750 m AVF, for the entire CROSSINN duration. The horizontal dashed black line indicates the location of Kolsass. The time resolution is 30 min. The yellow shaded regions indicate the regions used in the CVV identification algorithm. (b) Summary of the CVV identification algorithm results. Black rectangles denote the identified CVV 30-min intervals, while grey rectangles denote 30-min intervals characterized completely by precipitation, according to the ceilometer-based precipitation flag. The coloured labels correspond to IOP days: 8 August=IOP 2a; 9 August=IOP 2b; 14 August=IOP 4; 22 August=IOP 6; 13 September=IOP 8. (c) Time series of the SLXR142 horizontal wind speed between 0 and 1,000 m AVF $\langle U_{0-1000\text{m}} \rangle$ (shaded, blue), and 30-min intervals characterized by a downvalley flow (stippled, black). (d) Time series of the potential temperature difference $\Delta\theta$ between Hochhäuser and Kolsass [Colour figure can be viewed at wileyonlinelibrary.com]

in Figure 2a result primarily from low clouds or precipitation events, and more seldomly from one of the Windcubes being inoperational at the time (Figure 2b; Adler *et al.*, 2021d, their figure 5e).

The 750 m AVF transect reveals wide regions of updraughts above the southern sidewall and weaker, simultaneously opposing downdraughts above the northern sidewall. The two regions are on average symmetrical around Kolsass (Adler *et al.*, 2021d, their figure 10a). Such updraught/downdraught pairs occurred on a number of days in August, more rarely but with apparently equal intensity in September, and almost never in the first half of October. Given that these instances persisted continuously for many hours at a time, in some cases even during night-time, they cannot be due to daytime surface-driven convection alone. The prevalence of a stationary downdraught over the northern slope is further in disagreement with an expected greater positive heat flux over this slope than elsewhere in the valley (Lehner *et al.*, 2021), which would promote upward motion instead. Therefore, we hypothesize that these instances represent a dynamically driven CVV, generated by the slight curvature of the Inn valley (Figure 1a; Adler *et al.*, 2021d, their figure 10a,c).

We adopted the following set of criteria to extract 30-min cases with CVV. We focused on two regions of 1.5 km width above both valley sidewalls (yellow shaded regions in Figure 2a), for which we computed the average coplanar-retrieved u_z . First, we identified periods with a CVV as those 30-min intervals for which the southern u_z average was in excess of $0.35 \text{ m}\cdot\text{s}^{-1}$ and the northern average u_z was less than $-0.15 \text{ m}\cdot\text{s}^{-1}$. This step identified the most intense CVVs, although it may have missed the transient ones, for instance during onset and decay phases. Therefore, we identified additional potential CVV candidate periods as those remaining 30-min intervals with the same conditions as above, but with threshold values divided by four. These candidate periods were declared as CVV periods only if they preceded or were preceded by at least 1 hr of originally identified 30-min periods with CVV above. Lastly, we omitted those periods for which the areal coverage of the retrieved wind field was less than 20% of the largest possible coverage, here equal to the overall overlap among the three RHI fields within the retrieval grid (Figure 1b). Closer inspection of Figure 2b and the timing of all identified CVV cases, suggested that the majority occurred during daytime, specifically between 1200 and 2000 UTC. Therefore, we focus our attention on this period only.

The above criteria resulted in 132 30-min intervals classified as CVV, distributed among 23 days of the campaign (Figure 2b): thirteen in August, nine in September and one in October. Furthermore, four of these days corresponded to IOP days, specifically IOP 2a

(8 August), IOP 4 (14 August), IOP 6 (22 August), and IOP 8 (13 September). CVVs were most common between 1430 and 1530 UTC. It is worth noting that the number of 30-min periods classified as CVV showed a comparable sensitivity to both the choice of the identification level and the choice of average u_z thresholds. For instance, raising the identification level to 1,000 m AVF, resulted in a nearly twofold reduction of periods classified as CVV, thereby capturing only the deeper CVV structures. On the other hand, reducing the two u_z thresholds used above by $0.1 \text{ m}\cdot\text{s}^{-1}$ at the 750 m AVF level, resulted in a 40% increase of identified periods. However, some of these additional cases exhibited an extremely weak and broken-up downdraught region owing to the eased criteria, casting doubt on the apparent CVV structure typical of other cases found with our initial threshold scheme.

Lastly, it is instructive to explore the general thermodynamic conditions in the Inn valley during CROSSINN (Figure 2c,d). It is clear from Figure 2c that the majority of the periods with a CVV preferentially took place on days with a moderate to strong upvalley flow. Furthermore, a CVV took place not only during thermally driven daytime upvalley flow conditions, but also during the night with a synoptically forced upvalley flow, such as on 12 and 21 August, as well as 18 and 19 September. Days with weak upvalley flows or precipitation, for instance the period from 3 to 8 September, did not promote conditions to sustain a CVV. However days such as 22 August, with a strong upvalley flow but nearly no CVV cases identified, point to the fact that upvalley flow strength is likely not the only relevant parameter for CVV occurrence. On the other hand, consulting the potential temperature difference $\Delta\theta$ between Kolsass and Hochhäuser (Figure 2d), here taken as a proxy of low-level valley stability above Kolsass (Dreiseitl, 1988; Whiteman and Hoch, 2014; Haid *et al.*, 2020), reveals that the low-level valley atmosphere was unstable ($\Delta\theta < 0$) only during the transition from the night-time downvalley to daytime upvalley flow, usually between 0700 and 1500 UTC. Additionally, the length of the periods with negative $\Delta\theta$ progressively shortened over the course of the campaign, in accordance with gradually decreasing solar input. Unlike along-valley flow magnitude and direction (Figure 2c), $\Delta\theta$ suggests at first glance no relationship with periods with a CVV. This is in accordance with the earlier finding that CVVs occurred during night-time as well.

2.5.4 | Quantifying structural properties of a CVV

To illustrate the thought process behind quantifying CVV attributes, we focus on a 30-min afternoon period between

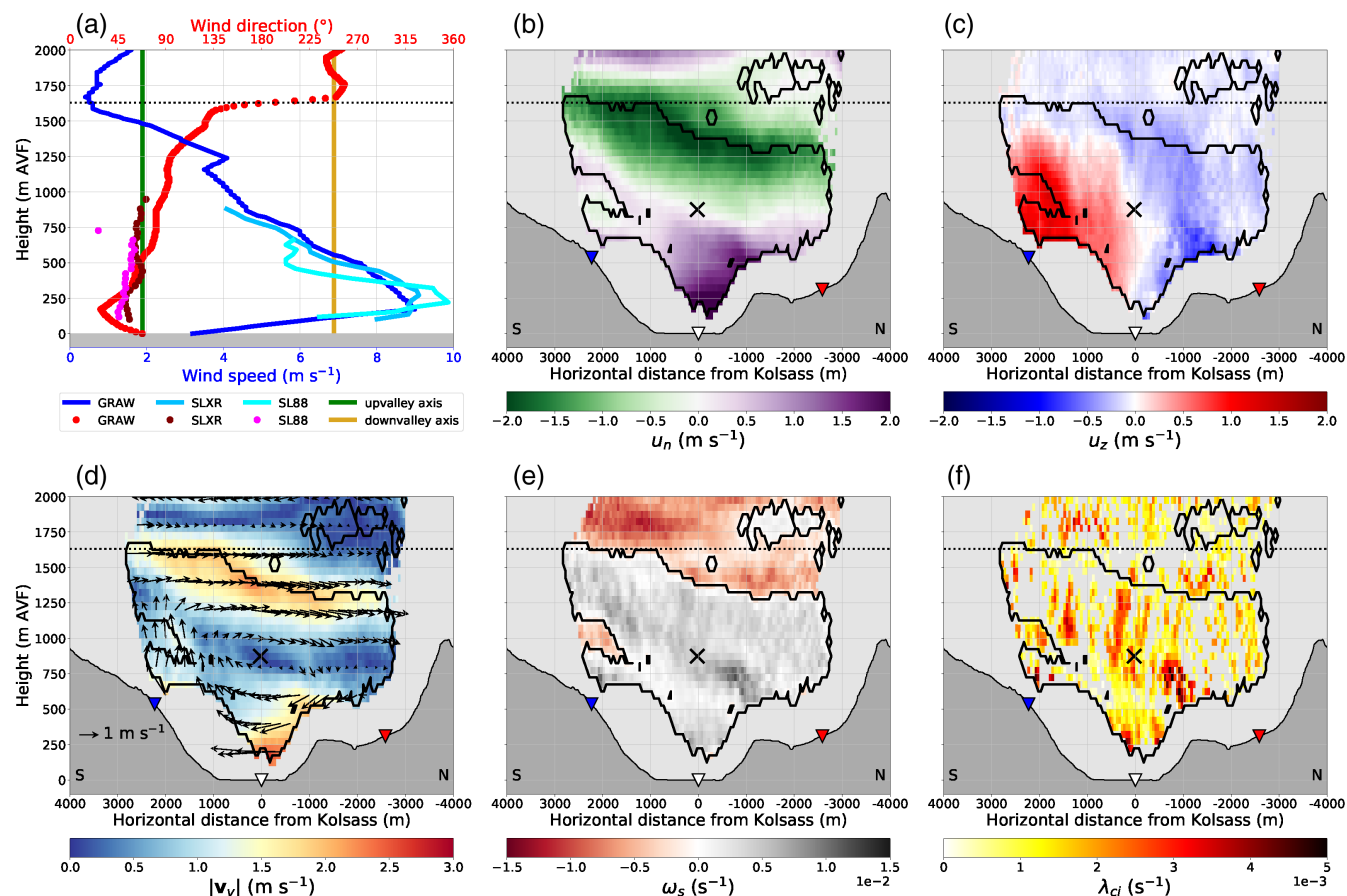


FIGURE 3 Visualisation of a typical 30-min period characterized by a CVV, for the time period 1600–1630 UTC on 14 August 2019 (IOP4). (a) Vertical profiles of wind speed and wind direction, shown collectively for the 1700 UTC GRAW radiosounding, the 1558:14 UTC VAD performed by the SLXR142, and the 1600:57 UTC VAD performed by the SL88. (b–f) are 30-min mean two-dimensional cross-valley fields, obtained from raw 1-min coplanar-retrieved data, of (b) cross-valley velocity component u_n , (c) vertical velocity component u_z , (d) quiver and shading representation of the total wind vector in the scanning plane $|v_v|$, (e) streamwise vorticity component ω_s , and (f) swirling strength λ_{ci} . The black contour lines in (b–f) represent outlines of the positive ω_s regions, while the X marks the CVV centre. Coloured triangles are the same as in Figure 1. The horizontal dotted black line indicates the altitude of the average ridgeline level equal to 1,630 m AVF [Colour figure can be viewed at wileyonlinelibrary.com]

1600 and 1630 UTC during IOP4 (Adler *et al.*, 2021d, Figure 3). The vertical profiles of horizontal wind speed and direction (Figure 3a) exhibited a low-level upvalley jet, and a clockwise veering with height that terminated at the ridgeline level. The wind direction, as obtained by the GRAW radiosounding, exhibited more rapid veering with height than the two VAD-derived profiles. Although this may be partly due to the sounding taking place 1 hr later than the two relevant Halo scans or due to the failure of the horizontal homogeneity assumption for VAD retrieval in complex terrain (Bingöl *et al.*, 2009), we consider it to be mainly a result of the sonde being advected further upvalley by the intense jet, therefore no longer being entirely representative for Kolsass.

We begin the CVV quantification with the coplanar-retrieved u_n and u_z components (Figure 3b,c). Below approximately 800 m AVF, the positive sign of u_n

indicates upvalley flow impinging onto the retrieval plane with a slight northerly angle (Figure 3b). Between 900 and 1,800 m AVF, the negative sign of u_n represents flow with a slight angle of attack from the south. This vertical variability of u_n with height is corroborated by Figure 3a, specifically by the clockwise turning of the upvalley wind. This clockwise shift with height was not constant across the valley, as indicated by the upward tilt of the upward boundary of positive u_n towards the southeast (Figure 3b). Furthermore, the spatial structure of the u_z component (Figure 3c) was, as expected, in agreement with the 750 m AVF transect used originally to detect CVVs (Figure 2a).

The cross-valley variability of $|v_v|$ offers evidence of the vortical nature of a CVV (Figure 3d). In other words, a CVV manifested as a clockwise vortex when looking upvalley, or equivalently, when looking downstream from the CROSSINN investigation area. The apparently larger $|v_v|$

near the surface and below the ridgeline level arose from the flow being least perpendicular to the retrieval plane there. This feature underscores the importance of properly interpreting angles of attack of the flow relative to the vertical scanning plane. This holds particularly for the upper levels, where the upvalley flow is noticeably weaker but aligned less along the upvalley axis than the lower levels (Figure 3a). Nonetheless, the high degree of comparability of the remotely sampled CVV structure with that obtained with FDLR measurements during this time period on IOP4 (Adler *et al.*, 2021d, their figure 10a,c), confirms the reliability of the coplanar retrievals for more advanced analyses.

Spatially abundant information of u_n and u_z enable quantification of relative vorticity (Holton, 2004):

$$\omega_s = \left(\frac{\partial u_z}{\partial n} - \frac{\partial u_n}{\partial z} \right), \quad (3)$$

where ω_s is the streamwise vorticity component. We emphasize that ω_s is the only relevant vorticity component for the present study, although it has to be kept in mind that it may possess small contributions from other (here neglected) vorticity components, due to the along-valley flow being never fully perpendicular to the retrieval plane. Below the ridgeline level, the dominating positive sign of ω_s is a result of the CVV clockwise sense of rotation in a right-handed natural coordinate system (Figures 1 and 3e). The uniformity of the ω_s patterns, or equivalently the lack of patchiness and intermittency within the predominantly positive ω_s , lends itself as a promising tool for delineating the spatial extent of a CVV. Given that many smaller regions of positive ω_s may exist, like those above the ridgeline level (Figure 3e), the one associated with the CVV needs to be identified first. To this end, all grid points simultaneously satisfying $|u_n| < 0.2 \text{ m}\cdot\text{s}^{-1}$ and $|u_z| < 0.2 \text{ m}\cdot\text{s}^{-1}$ are identified. Among those, the grid point with the minimum $|\mathbf{v}_v|$ is declared as the centre of a CVV (black X marker in Figure 3). The enclosed region of positive ω_s containing the CVV centre, therefore represents the CVV itself. Finally, we compute $\langle \omega_s \rangle$ as the spatially averaged streamwise vorticity ω_s inside the previously defined CVV region A .

To further characterize a CVV, the u_n and u_z retrieved wind fields can be used to obtain the period of a single revolution of a CVV around its streamwise axis. Similar to Hill *et al.* (2010), this can be accomplished by computing the two-dimensional form of the swirling strength λ_{ci} , following Chen *et al.* (2015):

$$\lambda_{ci} = \frac{1}{2} \sqrt{-4 \left(\frac{\partial u_n}{\partial z} \frac{\partial u_z}{\partial n} - \frac{\partial u_n}{\partial n} \frac{\partial u_z}{\partial z} \right) - \left(\frac{\partial u_n}{\partial n} + \frac{\partial u_z}{\partial z} \right)^2}, \quad (4)$$

and realizing that the desired period can be obtained as $T = 2\pi / \langle \lambda_{ci} \rangle$, where $\langle \lambda_{ci} \rangle$ is the spatial mean of λ_{ci} within the CVV area A . Interestingly, when considering the only other study reporting swirling strength in the MoBL, namely Hill *et al.* (2010) who studied subrotor vortices in the Owens valley, λ_{ci} of this particular CVV (Figure 3f) is one order of magnitude smaller than that of subrotor vortices (Hill *et al.*, 2010, their figure 7a). Such a comparison warrants caution, given that we compare two different types of vortex, specifically a streamwise vortex on the one hand (CVV) and a spanwise vortex on the other hand (subrotor vortex). Provided that a typical time-scale of a subrotor vortex lifecycle amounts to 5–8 min (Doyle *et al.*, 2009), the smaller order of magnitude of λ_{ci} would suggest that a CVV took on the order of tens of minutes to overturn around its streamwise upvalley axis.

Finally, we emphasize that not all CVV cases demonstrated a pattern as clean and consistent as that presented in Figure 3. Specifically, while a few cases exhibited extremely broken up or layered positive ω_s regions, others have potentially erroneously identified a CVV centre too close to the ridgeline level (not shown). To omit such suspicious instances not conforming to the prevailing structure, we first retained only those 30-min CVV cases whose centre fell inside a 2-km wide and 1-km tall region, centred above Kolsass. These boundaries are justified by the fact that the minimum $|u_z|$ typically occurred above or near Kolsass (Figures 2a). As a result, a total of four 30-min intervals were discarded, resulting in a total of 128 30-min intervals available for closer inspection.

3 | ENVIRONMENTAL CONDITIONS DURING CVV OCCURRENCE

In the following we explore the prevailing atmospheric conditions within and above the valley during CVV occurrences, with the aim of elucidating potential factors leading to a CVV. For brevity we focus only on conditions at Kolsass.

3.1 | Large-scale forcing

Major Alpine valleys such as the Inn valley have been shown to be potentially susceptible to the spatial distribution of large-scale pressure fields ultimately having an impact on along-valley flow via primarily pressure-driven channelling (Whiteman, 2000; Zängl, 2009). To explore the potential impact of the prevalent large-scale forcing on CVV during CROSSINN, we consulted ERA5 reanalysis fields of horizontal wind speed and direction above

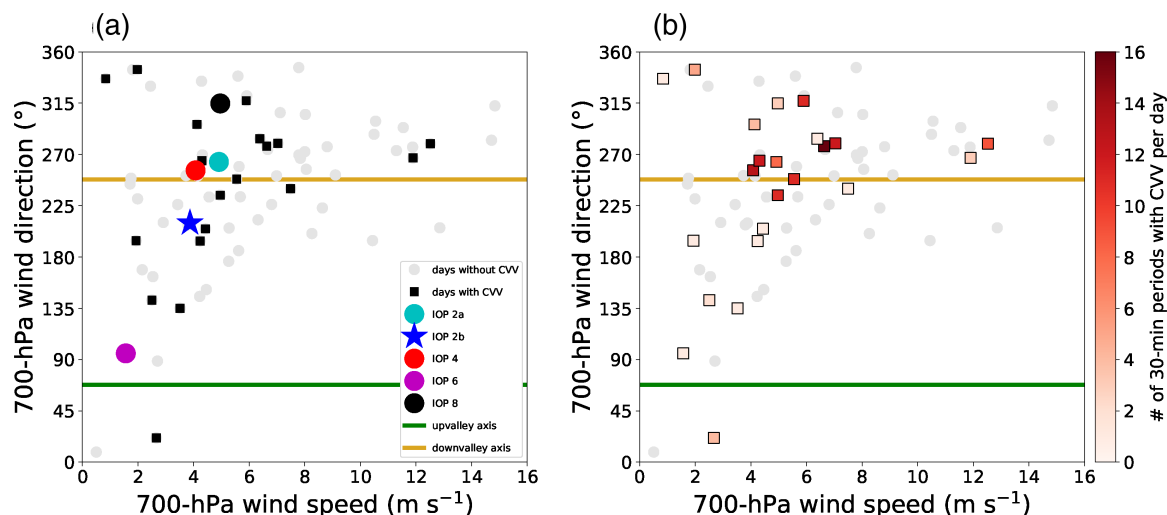


FIGURE 4 Mean (1200–2000 UTC) ERA5 wind speed versus wind direction for the grid point closest to Kolsass at the 700 hPa pressure level. In the case of wind direction, the average is obtained as a circular mean. The horizontal solid green and orange lines represent the upvalley and downvalley axes, respectively. In (a), upvalley wind days with a CVV are marked by black squares, while all other CROSSINN days are marked by grey circles. The IOP colouring convention is the same as in Figure 2b. In (b), the upvalley wind days with a CVV are colour-coded with respect to the total number of detected CVV 30-min periods on each day [Colour figure can be viewed at wileyonlinelibrary.com]

Kolsass, at the 700 hPa pressure level, for the period 1200–2000 UTC (Figure 4).

Moderate ($2\text{--}8\text{ m}\cdot\text{s}^{-1}$) flows with a westerly component ($180\text{--}360^\circ$) dominated above the investigation area during the majority of the CROSSINN campaign, in accordance with the assessment of large-scale forcing based on measurements from the Zugspitze mountaintop observatory as presented in Adler *et al.* (2021d), their figure 5a,b. Days with CVV spanned a large range of ambient wind speeds and directions, indicating a lack of preference for a certain type of ambient forcing (Figure 4a). The four IOPs with a CVV (Figure 2b) all fell within the range of wind directions between 240° and 90° , for which Zängl (2009) found had the weakest capacity to modulate the underlying upvalley flow. In the analyses to follow, we will focus also on IOP 2b, a representative upvalley flow day without a CVV. This upvalley flow day, unlike the other IOPs with a CVV, experienced a moderate large-scale southerly flow, resulting in a potentially disturbed upvalley flow with no CVV manifestations. This hypothesis will be scrutinized further in the sections to follow.

Although Figure 4a suggested a lack of preference for a type of ambient forcing, it ignored the information pertaining to persistence of a CVV on any given day. To account for this, Figure 4b demonstrates the total number of identified 30-min periods with CVV on each day. Such a representation reveals an evident clustering of days with longer-lasting CVVs for ambient forcings with a westerly fetch in excess of $4\text{ m}\cdot\text{s}^{-1}$. In other words, ambient winds of opposite fetch to that of the upvalley flow seem to

promote more longer-lasting CVVs. We postpone a more elaborate discussion of the potential implication of this counter-intuitive finding until Section 5.1.

3.2 | Atmospheric conditions at Kolsass

We computed the circular average surface wind direction at Kolsass to assess the conditions of the prevailing flow at that time (Figure 5a). We note that the more pronounced variability during night-time resulted from more variable flow conditions, belonging to either thermally driven downvalley flow or synoptically forced flow. Common for the 23 CVV days was the persistent northeasterly, upvalley flow from 1100 until roughly 2000 UTC (Figure 5a). Motivated by this finding, we decided to also explore the time evolution of other variables, and for all other upvalley flow days without any CVV. This step is motivated by the fact that all 23 CVV days were upvalley flow days, while on the other hand not all the upvalley flow days exhibited CVV occurrence. These days without a CVV, 31 in total, were declared as upvalley based on a subjective inspection of the prevailing along-valley flow direction from SLXR142 (not shown). We resorted to a subjective determination, given that ideal valley wind day classifications are often too strict (Lehner *et al.*, 2019; Adler *et al.*, 2021d). The upvalley flow fetch was, in both cases, slightly more northerly relative to our defined upvalley streamwise axis, more so on CVV days. In contrast to the similarity in flow direction, days with CVV were on average accompanied by as much as

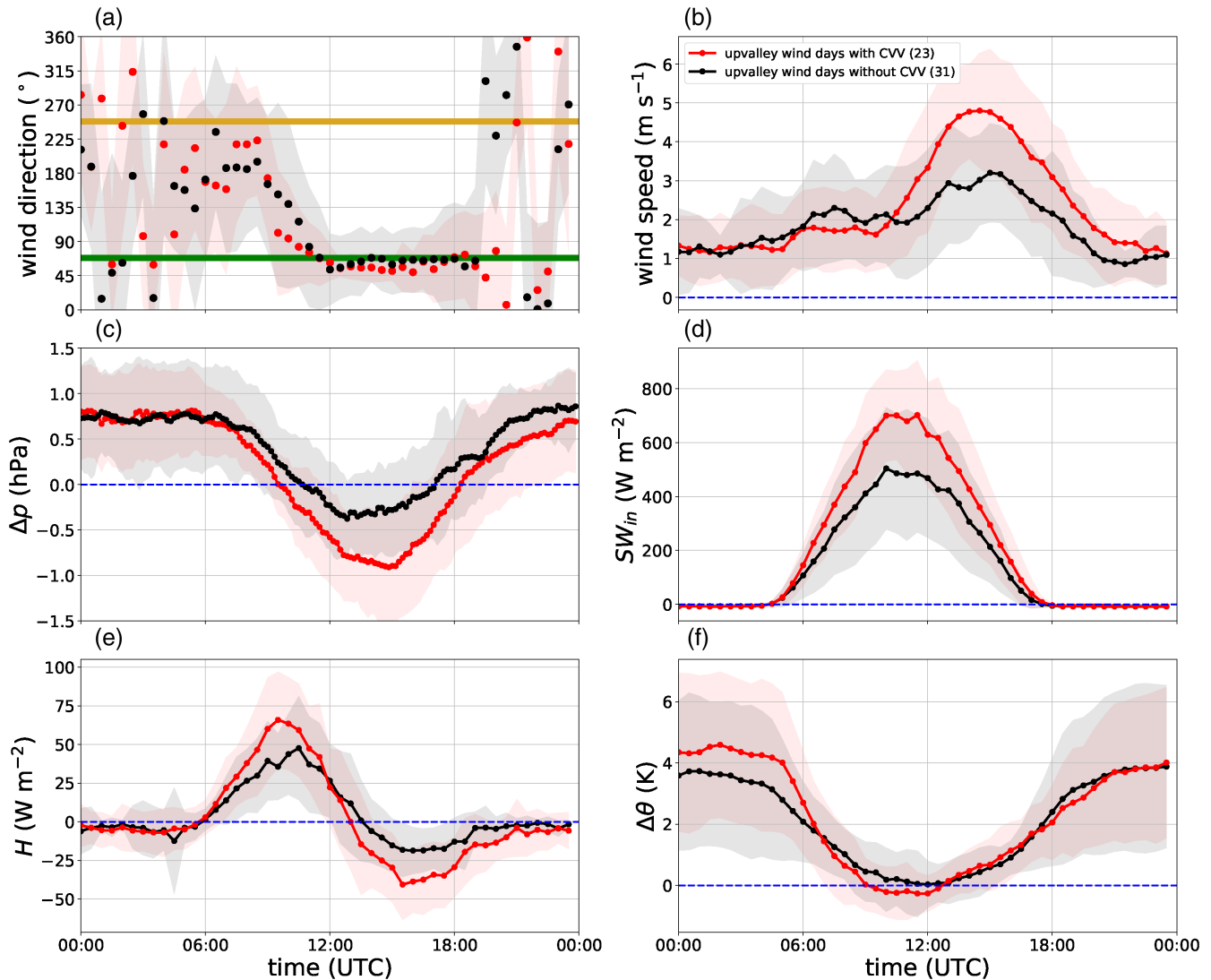


FIGURE 5 Time series of (a) wind direction at 8.7 m agl at Kolsass, (b) wind speed at 8.7 m agl at Kolsass, (c) pressure difference Δp between Kolsass and Kufstein, (d) incoming short-wave radiation SW_{in} at Kolsass, (e) sensible heat flux H at 8.7 m agl at Kolsass, and (f) potential temperature difference $\Delta\theta$ between Hochhäuser and Kolsass, including their respective standard deviations around the mean for upvalley wind days with (red) and without (black) CVV. Each data point is the mean composite of all days within the two categories. In the case of wind direction, circular means and standard deviations are shown. The horizontal dashed blue lines in (b–f) denote the zero value, while the horizontal solid green and orange lines in (a) denote the upvalley and downvalley axes, respectively [Colour figure can be viewed at wileyonlinelibrary.com]

60% more intense upvalley flows (Figure 5b). Furthermore, the peak upvalley flow at the surface, found between 1400 and 1600 UTC, coincided with the peak CVV occurrence (Figure 2b).

It is worthwhile to next explore the time evolution of the horizontal pressure difference between Kolsass and Kufstein, $\Delta p = p_{Kolsass} - p_{Kufstein}$; Kufstein is a city near the exit of the Inn valley (Figure 5c). Historically, the magnitude of this pressure difference correlated with upvalley flow strength on days with weak or even mild synoptic influence (Nickus and Vergeiner, 1984; Lehner *et al.*, 2019). Negative Δp during daytime hours, on the

order of -0.5 to -1 hPa for both IOPs, indicates a lower pressure at Kolsass than at Kufstein. This caused a horizontal pressure gradient force towards Kolsass, resulting in the upvalley flow.

Another significant discrepancy between the two day types can be observed in incoming short-wave radiation (Figure 5d) and sensible heat flux at the surface (Figure 5e), both displaying a greater magnitude on upvalley flow days with a CVV. We hypothesize that the overall greater radiation input drove a greater temperature and hence pressure contrast between the Inn valley and the Bavarian foreland, thus leading to a

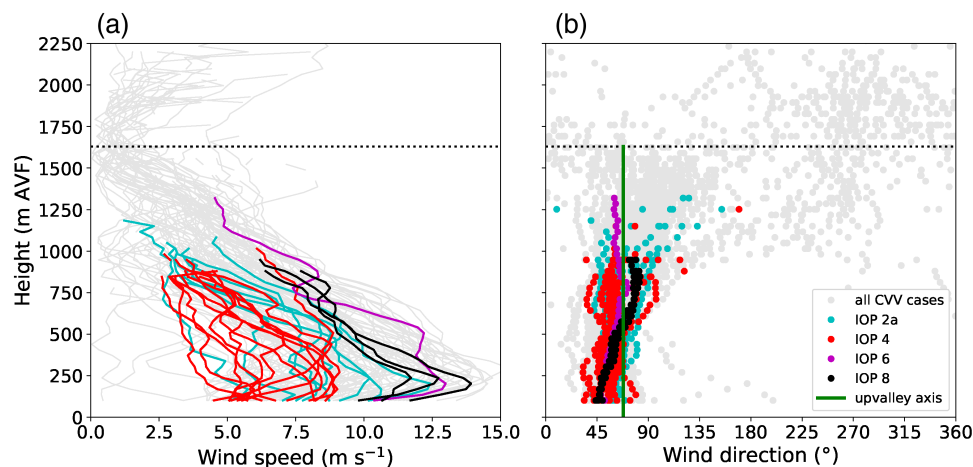


FIGURE 6 Vertical profiles of SLXR142 VAD (a) wind speed and (b) wind direction, for the matching 30-min intervals with a CVV. The IOP colour-coding convention is the same as in Figure 2b. The horizontal dotted black line indicates the altitude of the average ridgeline level equal to 1,630 m AVF. The vertical solid green line in (b) represents the streamwise axis [Colour figure can be viewed at wileyonlinelibrary.com]

stronger upvalley flow on days with a CVV (Nickus and Vergeiner, 1984; Vergeiner and Dreiseitl, 1987). The low absolute magnitudes of the sensible heat flux H , as well as the unusually early H sign reversal already at roughly 1300 UTC, resulted from much larger values of latent heat fluxes than H , not just at Kolsass, but at all three examined i-Box flux towers (Stiperski and Rotach, 2016; Lehner *et al.*, 2019; Lehner *et al.*, 2021), a feature common to many Alpine valleys. The short period of weak sensible heat flux, in turn, led to a shallow convective boundary layer (Ladstätter, 2020; Adler *et al.*, 2021d) and an early stabilisation of the valley atmosphere. In the Inn valley, it is also likely that the export of heat along the sidewalls, together with subsidence across the valley, may have additionally contributed to such a shallow and relatively short-lived convective boundary layer (Ladstätter, 2020). Figure 5f demonstrates the potential temperature difference between Kolsass and Hochhäuser $\Delta\theta$, shown already in Figure 2d. Owing to greater sensible heating of the valley atmosphere on days with a CVV, the potential temperature difference $\Delta\theta$ in the valley was negative between roughly 0900 and 1300 UTC on days with a CVV, which is not the case on days without a CVV for which $\Delta\theta$ values indicate neutral and even slightly stable conditions. However, one should keep in mind that the variability of H and $\Delta\theta$ for the two types of upvalley wind days significantly overlap, as evidenced by the shadings in Figure 5, pointing to the fact that, for instance, occasionally even days with strong surface heating and a more unstable atmosphere may not be accompanied by a CVV at all. In such cases, it is essential to focus on wind speed magnitude to help explain the lack of CVVs.

In summary, we found that an upvalley flow with a 30-min average in excess of 4 m s^{-1} (Figure 5b), a negative heat flux H from early afternoon onwards (Figure 5e), and an unstable preconditioning of the lower valley atmosphere prior to the onset of the upvalley flow (Figure 5e,f)

represent some of the possible indicators of a CVV at the valley floor at this slightly curved segment of the Inn valley.

3.3 | Characteristics of upvalley flow during CVV

Given that an upvalley flow appeared to have been an essential component for CVV occurrence (Figures 3a and 5a–c), we now determine the vertical structure of the upvalley flow above Kolsass, as inferred from the half-hourly profiles of horizontal wind speed from the SLXR142 (Figure 6).

The magnitude of the upvalley flow (Figure 6a) exhibited a consistent jet-like profile with height during CVV cases, with the jet height settling on average around 200–400 m AVF, and reaching values as high as 15 m s^{-1} . Based on the few cases during which SLXR142 measurements reached beyond the ridgeline level, it is also evident that the upvalley flow nearly vanished at or slightly above the average ridgeline level of 1,630 m AVF. When individual IOPs with a CVV are considered, it becomes clear that a CVV may persist for a large range of upvalley flow speeds. Interestingly, the fact that only one 30-min interval was identified as a CVV on IOP 6 (Figure 2b) is in contradiction with one of the strongest upvalley flows during CROSSINN sampled exactly on IOP 6. We will clarify this apparent conundrum in Section 5.1.

Similar to upvalley flow strength, the flow direction exhibited another largely consistent feature, namely a clockwise veering with height towards the ridgeline level (Figure 6b). Since the flow near the surface possessed a more pronounced northerly component relative to the streamwise axis (Figure 5a), upper levels then exhibited a slight southerly component relative to the streamwise axis. At the ridgeline level where the upvalley flow vanished,

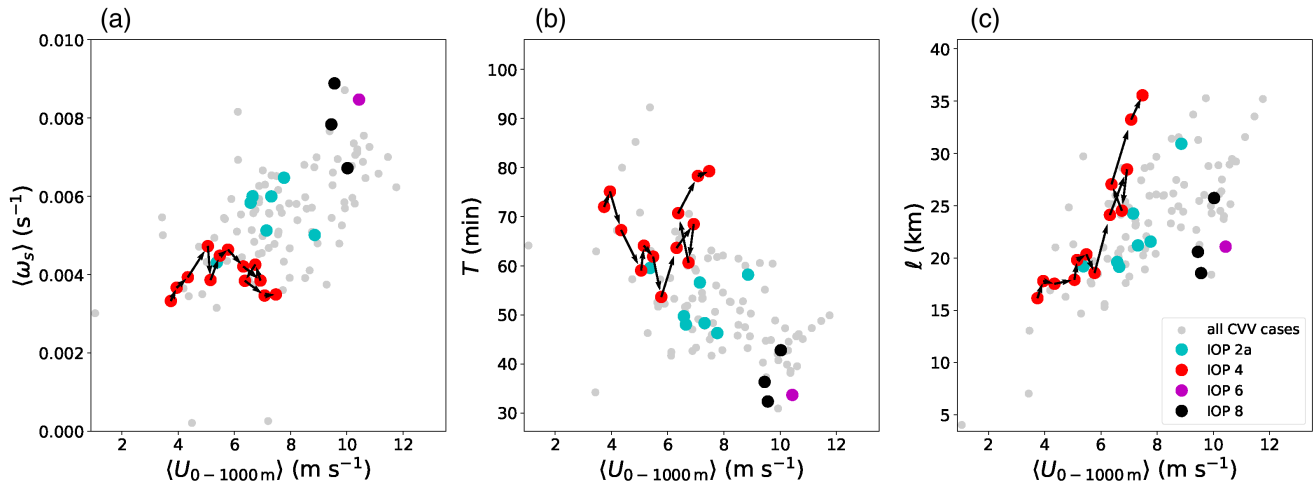


FIGURE 7 (a) CVV vorticity $\langle \omega_s \rangle$, (b) CVV overturning period T , and (c) CVV overturning distance ℓ , as a function of the SLXR142 bulk-valley mean horizontal wind speed between 0 and 1,000 m AVF. The IOP colour-coding convention is the same as in Figure 2b. The arrows connecting the IOP 4 30-min intervals with CVV represent time progression from 1200 to 1800 UTC, according to Figure 2b [Colour figure can be viewed at wileyonlinelibrary.com]

wind direction turned most often to westerly flow aloft, in agreement with Figure 4.

4 | RELATION OF CVV STRUCTURAL PROPERTIES WITH THE UPVALLEY FLOW STRENGTH

Having established the prevalent environmental conditions above and then below the ridgeline level, we now focus our efforts on determining the type of relationship between the structure of a CVV and the upvalley flow strength, determined previously to be a potentially important ingredient for CVV occurrence. By performing the computation of $\langle \omega_s \rangle$ and λ_{ci} for all 128 30-min intervals identified as CVV, we are now able to explore how the CVV is related to the intensity of the upvalley flow during CROSSINN. To quantify the latter, we computed the mean SLXR142 horizontal wind speed between 0 and 1,000 m AVF $\langle U_{0-1000\text{m}} \rangle$.

The overall near-linear increase of CVV vorticity with increasing horizontal wind speed (Figure 7a) reiterates the importance of the upvalley flow for the CVV. In other words, a CVV spins faster around its streamwise axis given a faster upvalley flow. The four IOPs agree with this conclusion to different extents.

In line with the previous conclusion made at the end of Section 2.5.4, the CVVs took longer than subrotor vortices to achieve a full revolution around their rotational streamwise axis, on average between 30 and 80 min (Figure 7b). Given that such a range of T corresponds to the time-scale of the MoBL sensitivity to surface forcing (Lehner and Rotach, 2018), a CVV qualifies as an

important phenomenon affecting exchange in the MoBL. The rotation period T was negatively correlated to the flow speed, thus leading to faster spinning CVVs for more intense upvalley flows. The CVV during IOP 4 revealed an inconsistent pattern, with an initial T decrease, followed by a further T increase with increasing wind speed. Closer examination of cross-valley transects of ω_s and λ_{ci} for those later early evening cases revealed that the CVV grew vertically until 1800 UTC, accompanied by a progressively smaller λ_{ci} (not shown).

The CVV period of a single revolution T allows us to determine at what distance downstream of the investigation area this revolution was achieved. To this end, we computed the CVV overturning distance ℓ by multiplying the CVV period T with $\langle U_{0-1000\text{m}} \rangle$. In this fashion, visualizing ℓ as a function of $\langle U_{0-1000\text{m}} \rangle$ suffers from self-correlation. Nonetheless, it is still reliable for determining the magnitude of ℓ , which amounted to 15–30 km during CROSSINN (Figure 7c). This finding implies that a CVV can be envisaged as a helicoidal, spiraling motion initiated at the valley curvature. However, we cannot pursue such an idealised visualisation hypothesis further, owing to the lack of similarly retrieved wind fields further up the valley.

5 | CVV MOMENTUM BUDGET AND DRIVING FORCES

Although the role of the upvalley flow strength has been substantiated in previous sections, another fundamental piece of information is still lacking, pertaining to the actual role of the curved segment of the Inn valley where the

CROSSINN investigation area was situated. Specifically, it remains unknown whether the advance of upvalley flow around this gentle bend is sufficient to drive a centrifugal force potent enough to generate a CVV. Therefore to address and answer our last scientific question, we focus on contrasting two IOPs with and without CVV, namely IOP4 and IOP2b (Figures 2b and 5). We first focus on establishing the main similarities and differences between the two IOPs, followed by the evaluation of the lateral momentum budget equation.

5.1 | Contrasting IOPs with and without CVV

Frequent GRAW radiosonde launches enabled a useful examination of the thermodynamic state of the MoBL during the two IOPs (Figure 8a,c). Common for both IOPs was an upvalley flow during daytime, as suggested already by Δp (Figure 5c). Additionally, a shallow, well-mixed boundary layer, and a moderate large-scale northwesterly and southwesterly flow during IOP4 and IOP2b,

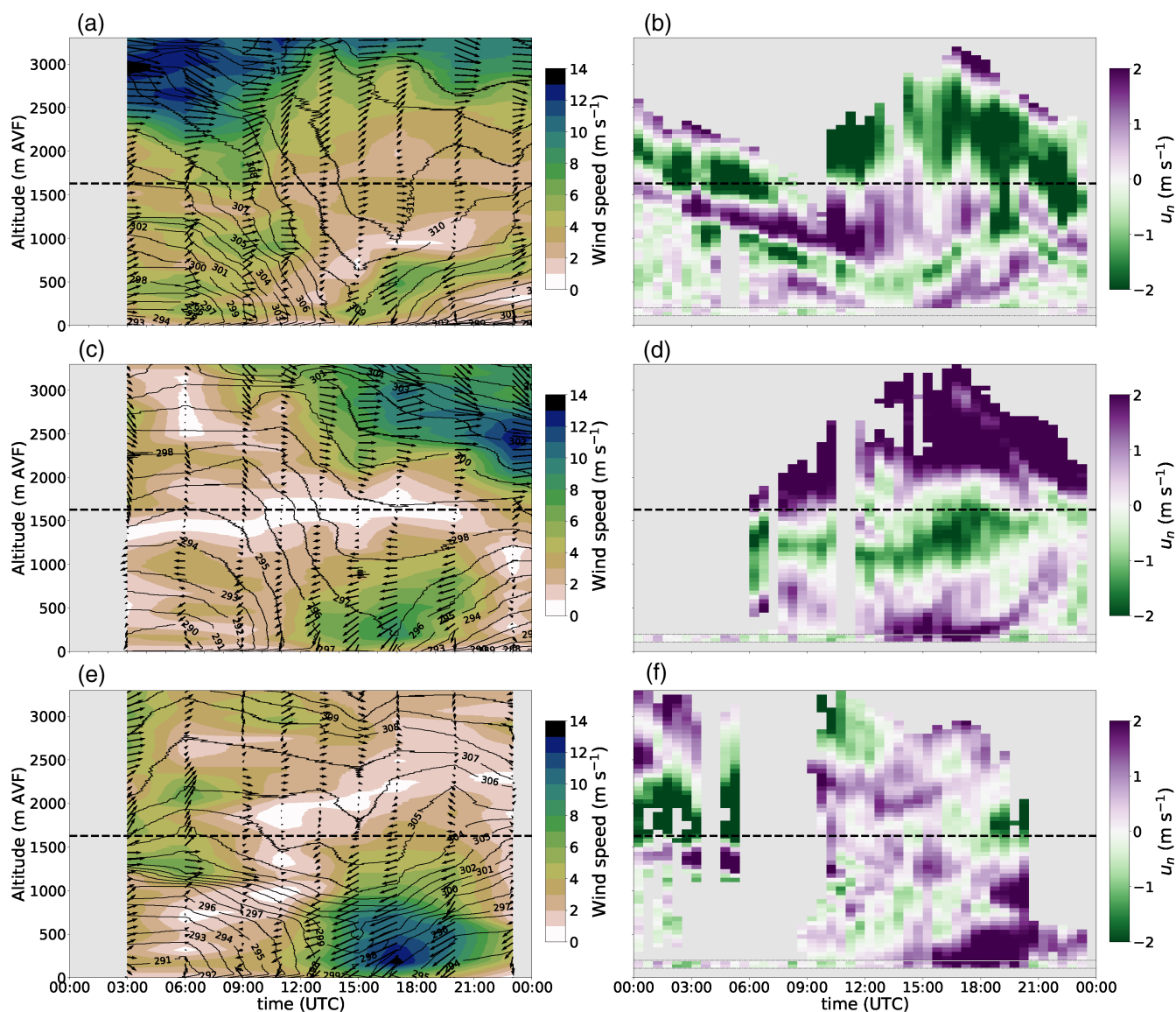


FIGURE 8 (a, c, e) Time-height representation of the GRAW wind speed (shading), GRAW isentropes (contours), GRAW horizontal wind vectors (arrows), and (b, d, f) time-height representation of the vertical profile of the cross-valley coplanar-retrieved velocity component u_n above Kolsass. In (b, d, f), altitudes between 118 and 200 m AVF show only the respective SL88 v component rotated into the natural coordinate system (Figure 1), while altitudes above 200 m AVF show only the matching coplanar-retrieved u_n component. For the SL88, the shown 30-min profiles were obtained as means from the original profiles sampled every 80 s. (a, b) represent IOP 2b, (c, d) IOP 4, and (e, f) IOP 6. The horizontal dashed black lines indicate the altitude of the average ridgeline level equal to 1,630 m AVF [Colour figure can be viewed at wileyonlinelibrary.com]

respectively (Figure 4; Ladstätter, 2020) were also common characteristics of both IOPs. Between approximately 0500 and 1000 UTC, the valley atmosphere experienced a gradual breakdown of the night-time surface inversion, as well as a weakening of the downvalley flow before the onset of the thermally driven upvalley flow around 1100 UTC on IOP 4 (Figure 8c) and 1400 UTC on IOP 2b (Figure 8a). Common for both IOPs was a gradual, bottom-up decay of the upvalley flow during the evening, driven by the stabilisation of the valley atmosphere (Figure 5e,f) and by a decrease in Δp (Figure 5c).

Based on the clockwise wind turning with height during CVV (Figures 3a and 7b), inspection of the vertical profile of the cross-valley wind speed component u_n directly above Kolsass (Figure 8b,d) provides a rough assessment of CVV presence without having to consult individual coplanar-retrieved wind fields (Figure 3b). The positioning of positive u_n close to the valley floor, with negative u_n concentrated in the upper half of the valley atmosphere (Figure 8d), agrees with the typical CVV structure (Figure 3b). During IOP 2b, such a vertical variation of u_n with height was limited to the shorter-lived and shallower upvalley flow, likely resulting in a very small CVV not captured by the 750 m AVF transect (Figure 2a). Unfortunately, such a small CVV cannot be confirmed by the coplanar-retrieved wind fields, since it likely populated the region rejected due to the intersection angle criterion close to the sidewalls.

As alluded to already in Sections 3.3 and 4, IOP 6 was marked by one of the strongest daytime upvalley flows during CROSSINN, yet only a single 30-min period was identified as a CVV. To address this, we inspect the thermodynamic state of the valley atmosphere in IOP 6 (Figure 8e,f), as previously done for IOPs 2b and 4 (Figure 8a–d). IOP 6 exhibited the deepest upvalley flow during CROSSINN which, based on late-afternoon radiosoundings, extended by roughly 600 m above the ridgeline level (Figure 8e). Simultaneously, as can be observed from the vertical profile of the cross-valley coplanar-retrieved wind speed component u_n between 1700 and 2000 UTC (Figure 8f), there was an erratic clockwise wind shift with height, compared to the more continuous shift observed for other CVV cases (Figure 6b). Such an anomalously deep upvalley flow, deviating from the usual termination at the ridgeline level during CVV occurrences (Figure 6a), resulted in a less spatially coherent clockwise vorticity structure (not shown). We hypothesize that, although the daytime upvalley flow is the governing driver of a CVV, whether a CVV actually develops may also depend on the ability of the large-scale forcing to prevent the upvalley flow from growing too deep (or, at the very least, to prevent the upvalley flow from exceeding the valley depth).

5.2 | Evaluation of the lateral momentum budget

The sufficiently strong and deep upvalley flow resulted in an uninterrupted 6.5-hr CVV in IOP 4. The lack of an upvalley flow with these attributes, in turn, helped corroborate the absence of a well-developed CVV during IOP 2b which could be detected. We hypothesize that this contrast between the two IOPs should be reflected in the cross-sectional representation of winds and scalars, as evident from the FDLR measurements. Furthermore, if the gradual valley curvature is indeed relevant for CVV generation, the two IOPs should be characterized by a different force imbalance. To substantiate this claim, we now turn to evaluating the lateral momentum budget in a natural frame of reference (Kalkwijk and Booij, 1986; Kim and Voulgaris, 2008; Nidzieko *et al.*, 2009):

$$\underbrace{\frac{\partial u_n}{\partial t}}_{LTT} = \underbrace{\frac{u_s^2}{R}}_{CGT} - \underbrace{u_s \frac{\partial u_n}{\partial s}}_{SAT} - \underbrace{u_n \frac{\partial u_n}{\partial n}}_{LAT} - \underbrace{u_z \frac{\partial u_n}{\partial z}}_{VAT} - \underbrace{\frac{1}{\rho_0} \frac{\partial p}{\partial n}}_{PGT} - \underbrace{f u_s}_{COT} - \underbrace{\frac{\partial \langle u'_n u'_z \rangle}{\partial z}}_{FRT}, \quad (5)$$

where s , n , and z represent streamwise, normal, and vertical directions, respectively, the curvature radius R equals 15 km, $g = 9.81 \text{ m} \cdot \text{s}^{-2}$ is the gravitational acceleration, $f = 1.07 \times 10^{-4} \text{ s}^{-1}$ is the Coriolis parameter for Kolsass, ρ_0 is the background air density, primes denote fluctuations about a time average, and brackets denote a time-averaged value (following Nidzieko *et al.*, 2009). The left-hand side represents the local tendency term (*LTT*), while on the right-hand side the terms are in order the centrifugal forcing term (*CGT*), the streamwise advective tendency term (*SAT*), the lateral advective tendency term (*LAT*), the vertical advective tendency term (*VAT*), the lateral pressure gradient forcing (*PGT*), the Coriolis forcing term (*COT*), and the frictional forcing term (*FRT*). With the current dataset available only across the valley, we are not able to compute *SAT*. Additionally, we cannot with sufficient confidence estimate *FRT*, provided that the relatively short length of the cross-valley legs would likely result in an underestimation of the $\langle u'_n u'_z \rangle$ momentum flux due to an insufficient convergence of its turbulent cospectrum. The two unknown terms define the residual term

$$\begin{aligned} RES &= SAT + FRT \\ &= LTT - CGT - PGT - LAT - VAT - COT. \end{aligned}$$

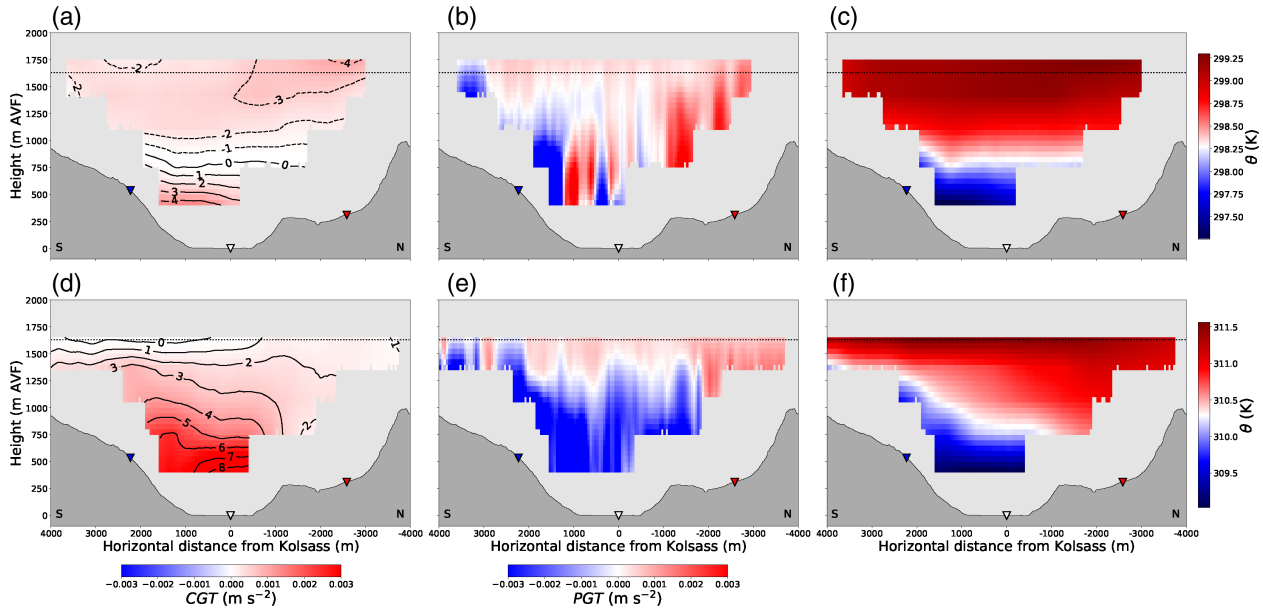


FIGURE 9 Cross-valley representation of the (a, d) centrifugal forcing term CGT , (b, e) pressure gradient forcing term PGT , and (c, f) potential temperature θ . In (a, d) the solid black contours represent the u_s wind speed component in the natural frame of reference (Figure 1) from which CGT is derived. The natural frame of reference applies only for the regions where the flow is upvalley, that is, where $u_s > 0$. Solid contour lines indicate upvalley flow, while dashed contour lines indicate downvalley flow. (a, b, c) represent IOP 2b, and (d, e, f) IOP 4. The horizontal dotted black lines indicate the altitude of the average ridgeline level equal to 1,630 m AVF. Coloured triangles are the same as in Figure 1 [Colour figure can be viewed at wileyonlinelibrary.com]

The Appendix S1 gives a detailed explanation of the evaluation of Equation (5), together with the computation of budget term uncertainties.

As shown in the SI, a scale analysis approach, as well as analysis of the FDLR data, revealed that the CGT and PGT terms represent the two leading-order terms in the lateral momentum budget during the examined cross-valley flights, particularly in IOP 4. While the CGT term is computed from the cross-valley field of u_s in a straightforward manner at each grid point (Figure 9a,d), the PGT term (Figure 9b,e) requires more attention. PGT is comprised of a baroclinic effect due to the flow super-elevation (Figure 9c,f), and of a barotropic effect owing to the pressure gradient forcing contribution along the ridgeline level, $PGT_{\text{ridgeline}}$. In discretized form, PGT can then be expressed as (Lacy and Monismith, 2001; Kim and Voulgaris, 2008; Nidzieko *et al.*, 2009):

$$\begin{aligned}
 PGT &= \frac{g}{\theta_0} \int_z^{h_{\text{fifth leg}}} \frac{\partial \theta'(z')}{\partial n} dz' + PGT_{\text{ridgeline}} \\
 &= \frac{g}{\theta_0} \left[\frac{\Delta z}{2\Delta y} \left(\sum_{i=1}^m \theta'_{i,j+1} - \sum_{i=1}^m \theta'_{i,j-1} \right) \right] + PGT_{\text{ridgeline}},
 \end{aligned}
 \quad (6)$$

where $\Delta y = \Delta z = 50$ m are the cross-valley and vertical mesh spacings, respectively, θ' is defined as the perturbation from the cross-valley mean potential temperature

at each Δz height AVF, θ_0 is the mean potential temperature at the top of each considered depth cell, m is defined as the index of the corresponding depth cell for which PGT is calculated (Nidzieko *et al.*, 2009), i and j are the dummy vertical and lateral indices, respectively, and $h_{\text{fifth leg}}$ is the height AVF of the respective flight leg closest to the average ridgeline level. The SI gives details on the uncertainties of these two terms.

During IOP 2b, the upvalley flow was significantly shallower and weaker than in IOP 4 (Figures 8 and 9a), not exceeding 800 m AVF at the time of the FDLR flight. This limited the extent over which the natural frame of reference is valid, on which the budget relies, to altitudes below 800 m AVF (Figures 9a and 10a). On the other hand, the PGT exhibited a spatially patchy behaviour, with both positive and negative signs. This is a result of the general lack of a flow super-elevation effect in IOP 2b (Figure 9c), given the rather weak upvalley flow (Figure 9a). There, the two terms that are expected to be dominant for CVV development, namely CGT and PGT , were comparable to the other terms in order of magnitude. This indicates a lack of the necessary force imbalance with height, and therefore a lack of a CVV that could be detected during IOP 2b.

In IOP 4 (Figures 9d–f and 10b), CGT and PGT represented the leading-order terms with largest magnitudes over the majority of the valley depth, with CGT being responsible for accelerating the flow towards the southern

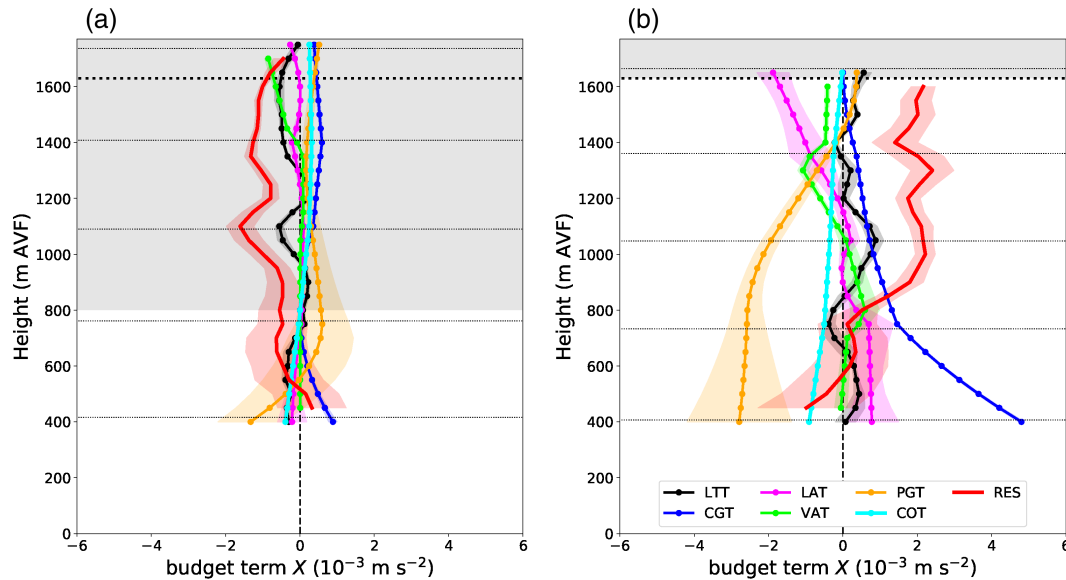


FIGURE 10 Vertical profiles of the terms of the lateral momentum budget for (a) IOP 2b and (b) IOP 4. Each line corresponds to the mean of a 500-m wide section of the 2D field of each term, centred at Kolsass. The coloured shaded regions indicate \pm one standard deviation around the respective term resulting from such spatial averaging. The budget terms correspond to the local tendency term *LTT*, lateral advection term *LAT*, vertical advection term *VAT*, centrifugal acceleration term *CGT*, Coriolis acceleration term *COT*, pressure gradient term *PGT*, and the residual term *RES*. The vertical dashed black line indicates zero acceleration, the horizontal thick dotted black line indicates the altitude of the average ridgeline level equal to 1,630 m AVF, and the horizontal thin dotted black lines indicate the altitudes of the five analyzed cross-valley legs. The grey shaded regions denote the height ranges in which the flow is not upvalley ($u_s < 0$) [Colour figure can be viewed at wileyonlinelibrary.com]

sidewall in the lower half of the valley, while *PGT* accelerated the flow toward the northern sidewall in the upper half of the valley. Unlike IOP 2b, the flow superelevation effect was far more pronounced in IOP 4, as evident from the piling of potentially colder air over the southern sidewall (Figure 9f). As the ridgeline is approached from lower levels, the relative importance of *CGT* and *PGT* gradually weakened. Although other terms were of significantly smaller magnitude above Kolsass, they became comparable to *CGT* and *PGT* over the valley sidewalls, particularly *VAT* (Figure S5).

6 | DISCUSSION

Here we provide a qualitative comparison between CVV and the secondary circulation observed in water channels and in the Riviera valley (WR04). Finally, we present the reader with a conceptualized lifecycle of a CVV in the CROSSINN investigation area.

6.1 | Comparison with the Riviera valley and other curved channel flows

A vertical imbalance between the centrifugal and pressure gradient forces led to a CVV in the CROSSINN

investigation area (Figure 11a). Looking upvalley, the Inn valley bends to the right and the CVV is clockwise, with the lower branch pointing from the inside of the bend towards the outside, and the opposite holding for the upper branch of the vortex (Figure 11b). As pointed out in Section 1, the only other experimental evidence for a CVV in the atmosphere is from the MAP campaign in the Riviera valley in Switzerland (WR04). In their case, the upvalley flow passing through a left-hand bend also generated a clockwise secondary circulation, however, with the lower and upper branches pointing in the opposite directions than in the Inn valley (Figures 11b,c). WR04 similarly hypothesized that it was the vertical imbalance of the centrifugal and pressure gradient forces leading to the CVV (WR04, their figure 11). They used a simplified conceptual model with a constant *PGT* with height and a centrifugal force (*CGT*) that increases with height due to generally increasing wind speed (Figure 11d). This conceptual model was motivated by hydrological flows in meandering channels (see below). However, due to the much coarser spatial resolution of their observations (in particular, no cross-valley lidar retrievals of the relevant variables), they did not explicitly determine these profiles (as in Figure 10).

Despite the limited database, we have attempted to re-analyze the Riviera data in order to retrieve the profiles for at least the *PGT* and *CGT* terms in a similar fashion as presented for the Inn valley in Figure 10. The results

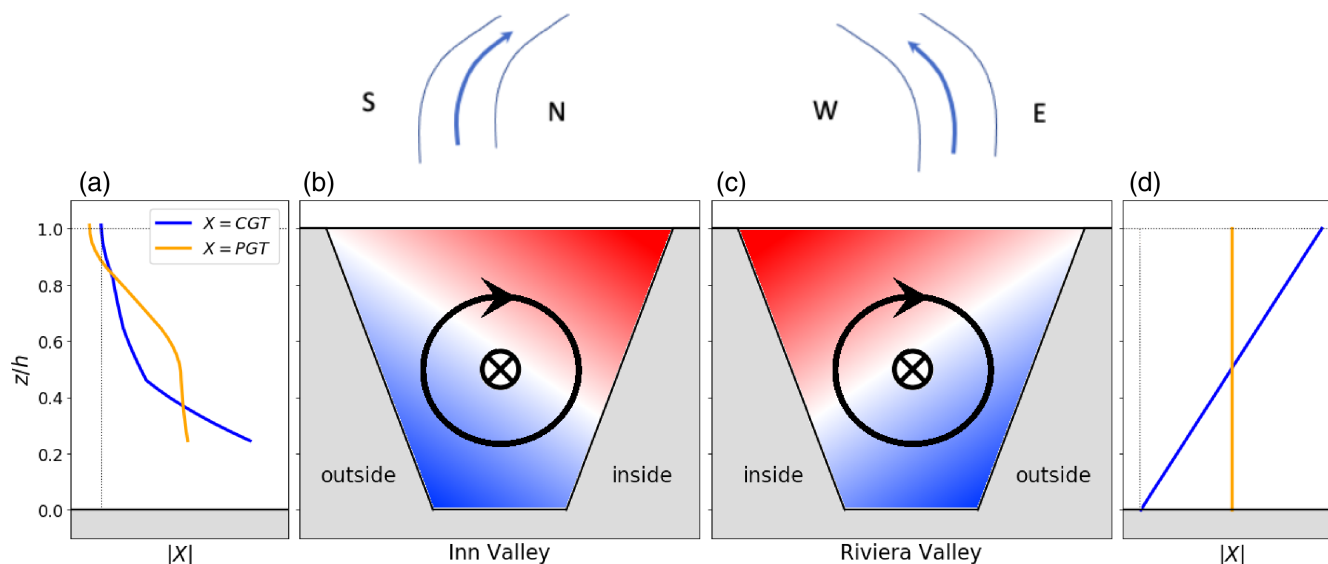


FIGURE 11 Schematic summary of prevailing conditions driving a CVV in the Inn and Riviera valleys. (a) Vertical profile of absolute lateral momentum budget terms $|X|$ for the CROSSINN investigation area, (b) cross-section of the CROSSINN investigation area, (c) cross-section of the Riviera valley, and (d) vertical profiles of absolute lateral momentum budget terms $|X|$ for the Riviera valley (following WR04, their figure 11). The vertical axes represent the vertical coordinate normalized by the valley depth h . Horizontal dotted lines represent the ridgeline level, while the vertical dotted lines in (a, d) denote zero acceleration. In (b, c), the crossed-out circle denotes flow direction up the valley, the black circles with arrow indicate the sense of rotation of the CVV, the *inside* and *outside* labels indicate locations of the respective sides of the bend at the cross-section, and the shaded regions represent the cross-sectional distribution of potential temperature, with lower values represented by colder colours. The two sketches at the top of (b, c) refer to the bending of the two valleys with flow direction during daytime [Colour figure can be viewed at wileyonlinelibrary.com]

(not shown) indicated that the proposed model for the sense of rotation in the Riviera CVV was oversimplified, that is, that the two terms did not to first order dominate the momentum balance in the valley atmosphere, with a change in sign of their relative importance ($|PGT| - |CGT|$) at a mid-valley level (Figure 11d). Unfortunately no information is available to judge which of the other terms in Equation (5) – likely advection – might have impacted the balance. We emphasize that the sketch presented by WR04 (reproduced here as Figure 11d), may have oversimplified the extent of the observed vertical structure of the upvalley flow in the Riviera valley. However, WR04 drew their conclusions on the origin of the CVV based on only a few selected fair-weather days when aircraft data (only three flight legs across the valley at each height) were available. In the present study, in contrast, we have a 2.5-month period to demonstrate the persistence of the low-level upvalley jet in the Inn valley and additionally the *in situ* aircraft measurements during the IOPs to investigate nearly all terms in the lateral momentum budget.

Nevertheless we look at similarities and differences between the CVV in the Inn and Riviera valleys. In both cases, the centrifugally induced accumulation of potentially colder MoBL air on the outside of the bend led to a cross-valley potential temperature gradient, driving

a pressure gradient force back towards the inside of the bend (Figure 11b,c). Therefore, we hypothesize that the reason for the conflicting sense of rotation between the two valleys lies in the shape of the vertical profile of the centrifugal force (Inn valley, Figure 10), or the sum of the *CGT* term with other term(s), which cannot be quantified from the available Riviera observations. In other words, it appears that the vertical profile of the upvalley flow is crucial for the sense of rotation of a CVV. In the Riviera valley, the wind profile – in concert with other terms – appears to have produced a net vertically increasing momentum forcing (blue $|X|$ term in Figure 11d). In the Inn valley, conversely, the upvalley flow is characterized by a low-level jet (Figures 3a, 6a and 8c) thus leading to a different sense of rotation for the CVV than expected from the simple model of the ‘meandering channel flow’.

Different mean flow profiles have been found to influence the sense of rotation in other – otherwise comparable – flows. It is well known in marine hydrology that subaerial channels, such as rivers, estuaries and marshes (Geyer and MacCready, 2014) exhibit a distinctly different vertical along-channel flow profile than that encountered in submarine channels (Peakall and Sumner, 2015). While a nearly continuous increase of along-channel flow strength to the surface of rivers is one of their most documented features, a profile typical

for a gravity current with a low-level jet represents a universal feature of nearly all submarine channel flows (Corney *et al.* 2006, 2008). Although lateral salinity, density and sediment gradients become relevant in water flows (Azpiroz-Zabala *et al.*, 2017), the different vertical profiles of along-channel flow have been postulated as one of the main reasons why secondary circulations in subaerial and submarine channels often exhibit opposite senses of rotation for a given channel bend orientation (Corney *et al.*, 2008; Giorgio Serchi *et al.*, 2011). For a range of different vertical profiles of along-channel flow, Corney *et al.* (2008) found two different flow regimes: if the flow maximum is located close to the bottom ($z/h \approx 0$) or the top ($z/h \approx 1$) of the channel, the vertical profiles of the cross-channel velocity component (Figure 8b,d) exhibit opposite signs (Corney *et al.*, 2008, their figure 2). For the case of a flow maximum at around $z/h = 0.5$, two stacked circulation cells with opposing rotation senses are possible.

6.2 | Conceptual CVV daily and seasonal lifecycle

The gentle valley bend in the investigation area was sufficient to generate a CVV given an intense upvalley flow with a pronounced low-level jet, with its depth limited to below the average ridge height. Here we illustrate the three distinct stages of the MoBL in the investigation area on a typical upvalley day when a CVV was present. On a fair-weather summer day with moderate synoptic forcing (Figure 4), upslope flows dominate the period between the transition from night-time downvalley to daytime upvalley flow (Adler *et al.*, 2021d, their figure 7c,d). At this time during late morning and early afternoon, the sensible heating is at its maximum (Figure 5e), promoting upslope flows over both valley sidewalls.

As the temperature and hence the pressure contrasts between the Inn valley and the Bavarian foreland continue to amplify (Figure 5c), upslope flows become overpowered by an upvalley flow. The valley gradually stabilises as a result of negative sensible heat flux (Figure 5e,f), while the upvalley flow simultaneously gains in both depth and intensity (Figures 5b and 8d). Such a strengthening upvalley flow induces a centrifugal force towards the southeast, piling up potentially colder air above the southern valley sidewall (Figures 11b). The established cross-valley temperature gradient generates a pressure gradient force opposing the centrifugal force (Figure 10b), leading to a clockwise CVV when looking upvalley (Figure 3d). As long as the upvalley flow remains sufficiently strong and approximately 1,700 m deep (Figures 6a and 8c), the CVV may persist for several hours (Figure 2b). The CVV itself is

therefore purely dynamically driven by the upvalley flow, despite a negative sensible heat flux at the surface. Given the lack of adequate observational coverage of the valley atmosphere between the CROSSINN investigation area and Innsbruck, it is hypothesized that the CVV manifests as a spiraling motion further upvalley (Figure 7c), overturning once around its streamwise axis at a distance of 15–30 km.

With a progressively smaller solar input during the evening hours (Figure 5d), along with further valley stabilisation (Figure 5e,f), the temperature and hence pressure contrasts between the valley and foreland weaken, resulting in a weakening of the upvalley flow (Figure 5b,c). Simultaneously, the low-level upvalley flow jet decouples from the surface and lifts towards higher altitudes (Figure 8c). Accompanying the weakening and lifting off of the upvalley flow, the CVV simultaneously loses its structural integrity (Figure 8d) and disappears with the cessation of the upvalley flow.

Lastly, it is worth addressing the seasonal presence of a CVV in the Inn valley. Due to the strong link between a CVV and upvalley flow strength, it is rather unlikely that a CVV occurs during late autumn, winter and early spring months. This became evident from Figure 2b, showing a decrease of upvalley wind days with a CVV from August to October. Both the duration and intensity of upvalley flow decrease significantly during winter (Vergeiner and Dreiseitl, 1987, their figure 4; Zängl, 2004, his figure 10e), indicating a low likelihood of CVV formation. Further evidence for a lack of a CVV during wintertime can be found in Gohm *et al.* (2009), who analyzed aircraft and remote-sensing data along a cross-valley transect on the opposite side of the present valley curvature. In addition to a weaker and shallower upvalley flow (Gohm *et al.*, 2009, their figure 9c) than the one observed during IOP 2b (Figure 8a), the observed circulation in their case was layered, showing an opposite sense of rotation compared to a CVV, not fully closed, and buoyantly driven by asymmetrical heating of the valley sidewalls (Gohm *et al.*, 2009, their figure 10c).

7 | SUMMARY AND OUTLOOK

We conducted a 2.5-month field campaign called CROSSINN during summer 2019 in a slightly curved segment of the Inn valley, centred around the i-Box long-term flux measurement network approximately 18 km east of Innsbruck. By utilizing measurements from five Doppler lidars, a ceilometer, *in situ* aircraft, radiosounding and surface eddy-covariance observations, collected in a region of horizontally heterogeneous and complex terrain, we obtained a unique insight into the three-dimensional

kinematic structure of the MoBL around the valley curvature. The cornerstone of the campaign was the knowledge of the two-dimensional wind across the valley, obtained using a coplanar retrieval algorithm applied to RHI scans from three Doppler lidars. The goal of the present study was to determine the prevailing conditions found during CVV occurrence, to determine the degree to which upvalley flow shape and strength dictate CVV occurrence, and to determine whether the lateral momentum budget force imbalance explains the observed (and lack of) CVV pattern.

A CVV was marked with large and temporally stationary regions of updraughts and downdraughts above the southern and northern valley sidewalls, respectively. Looking upvalley, this resulted in a clockwise circulation spanning the entire valley depth. CVVs mostly occurred during an 8 hr period between 1200 and 2000 UTC, on a total of 23 upvalley flow days of the campaign. The vertical profile of the upvalley flow exhibited, across all identified cases of CVV presence, a low-level jet maximum at around 400 m AVF, a minimum wind speed slightly above the ridgeline level, and clockwise veering with height. Given a predominantly negative sensible heat flux across the valley surface, together with a stabilising valley atmosphere, the CVV was mainly dynamically driven. Quantification of vorticity-based parameters using coplanar retrievals, revealed a positive correlation between vorticity and upvalley flow strength, and an overturning period on the order of 30 to 80 min. An additional outcome of this vorticity-based analysis was the hypothesis that CVVs overturn once within a distance of 15–30 km further up the valley. Evaluation of the lateral momentum budget, using *in situ* aircraft measurements collected during IOPs 2b and 4, revealed the importance of the interplay between centrifugal forcing and pressure gradient forcing. While the former dominated the latter in the lower half of the valley cross-section, the opposite held for the upper half of the valley, explaining the observed clockwise sense of rotation. Once the upvalley flow began to weaken in the evening, its upvalley jet exhibited a bottom-up lifting, leading to a gradual decay of the CVV. Comparison with the observational evidence of a CVV in the Riviera valley (WR04) revealed the importance of the vertical profile shape of the upvalley flow, thus helping to explain the same sense of rotation despite the two valley curvatures bending in different directions. Furthermore, closer inspection of IOP6 revealed the importance of a westerly large-scale forcing preventing the upvalley flow from becoming too deep. Ultimately, a CVV can be regarded as a hybrid MoBL phenomenon, exhibiting both thermally driven traits (because of its dependence on a thermally driven upvalley flow) and dynamically driven traits (owing to the valley curvature).

The study of a CVV in the Inn valley, which owes its novelty to coplanar-retrieved wind fields obtained with largest areal and temporal coverages to date, suggests multiple research venues worth exploring next. The challenge of deploying Doppler lidars in complex terrain restricted our analysis to a single cross-valley transect, leaving incomplete information regarding the evolution of the upvalley flow across the entire length of the curvature. By obtaining multiple snapshots of cross-valley flow structure along the curvature and even further upvalley by means of aircraft measurements, a more complete picture of a CVV can be obtained to better quantify its impact on the MoBL characteristics. Presently, we were unable to explore four additional aspects with the present dataset. First, it remains unknown whether upvalley flow impinging onto the southwestern tributary Weer valley sidewall may have led to an amplification of the CVV updraught branch (Figure 1a; Adler *et al.*, 2021d, their figure 11a). On the other hand, the Weer valley could have exerted a tentative negative impact on CVV, through leakage of potentially colder air up the Weer valley, diminishing the superelevation effect and thus the resulting pressure gradient force. These questions can be addressed by means of measurements collected deeper into the Weer valley, as well as using semi-idealized numerical simulations in which the Weer valley can be artificially removed to determine the actual extent of its impact on the CVV. Specifically, a large-eddy simulation with a horizontal resolution on the order of 150 m and finer would be well suited for this task (Weigel *et al.*, 2006; Cuxart, 2015; Umek *et al.*, 2020). Second, it is unclear from the CROSSINN observations at what point upstream of Kolsass the CVV was actually initiated. Third, although the occurrence of a counter-clockwise CVV during downvalley flow is far less likely compared to the upvalley cases, it would nonetheless be fruitful to explore these in more detail, given that downvalley flows are both more frequent and longer-lasting during winter months when extreme pollution episodes are also more detrimental (Zängl, 2004; Gohm *et al.*, 2009; Harnisch *et al.*, 2009). Fourth, the actual impact of a CVV on the exchange of scalars, such as heat and moisture, in the MoBL remains unclear, an aspect we assume to be related to the hypothesized elongation of a CVV downstream of Kolsass. Lastly, we point out the necessity of exploring the capacity of other curved valleys for sustaining CVVs. In case of broader valleys, we suggest deploying a line of Doppler lidars along the valley floor through and downstream of a valley curvature, and setting them to perform VAD scans on a routine basis. The cross-valley wind component obtained with such scans can then be used as a proxy for the presence of CVVs (Figure 8b,d,f). Although the applicability of horizontal homogeneity on which the traditional VAD algorithm is based becomes violated in

complex terrain (Bingöl *et al.*, 2009), performing them away from the sidewalls, as in the present study (Figure 6), alleviated some of this disadvantage owing to the decent degree of comparability with the *in situ* radiosonde wind measurements (Figure 3a). If curved narrower valleys are under scrutiny for the suspicion of the presence of CVVs, performing the same coplanar retrieval strategy as in the present study, but with only two Doppler lidars, should allow for greater flexibility in reassigning the role of the third Doppler lidar.

The underlying idea behind CROSSINN, to sample the three-dimensional flow structure across a valley using state-of-the-art instrumentation from long-term networks (i-Box) and mobile instrument platforms (KITcube), falls within the scope of the next major complex terrain endeavour, namely the Multi-scale transport and exchange processes in the atmosphere over mountains (TEAMx) programme and experiment (Serafin *et al.*, 2020). If the Inn valley, specifically the CROSSINN investigation area, is likely to be one of the major targets of TEAMx efforts, the findings presented in this study, along with the above remaining questions, will undoubtedly assist in better planning and in overcoming logistical challenges.

ACKNOWLEDGEMENTS

We thank the two anonymous reviewers for their valuable feedback, which led to a significant improvement of the manuscript. CROSSINN was funded by the Deutsche Forschungsgemeinschaft (DFG, German Research Foundation) – 406279610. The DLR Cessna Grand Caravan 208B flights have been kindly financed by the Karlsruhe Institute of Technology (KIT). Part of University of Innsbruck's contribution was financed through the research project PIANO funded by the Austrian Science Fund (FWF) and the Weiss Science Foundation under grant P29746-N32. We thank all CROSSINN participants for their field and data processing assistance, including Karmen Babić, Shweta Singh, Timo Gamer, Martin Kohler, Simone Scheer, and Andreas Wieser from KIT, as well as Gaspard Simonet, Maximilian Stärz, Lukas Lehner, and Manuel Saigger from the University of Innsbruck. We acknowledge Christian Mallaun from DLR, for providing the quality-controlled FDLR measurements. Special thanks go to Hubert Dengg in Hochhäuser and the owners of the Rantner riding stable in Mairbach for allowing the equipment to be installed in their grounds.

AUTHOR CONTRIBUTIONS








Nevio Babić: conceptualization; data curation; formal analysis; investigation; methodology; supervision; visualization; writing – original draft; writing – review and editing. **Bianca Adler:** conceptualization; data

curation; funding acquisition; project administration; supervision. **Alexander Gohm:** conceptualization; data curation; funding acquisition. **Norbert Kalthoff:** conceptualization; supervision. **Maren Haid:** conceptualization; data curation; methodology; resources. **Manuela Lehner:** conceptualization; data curation; resources. **Paul Ladstätter:** conceptualization. **Mathias W. Rotach:** conceptualization; visualization; writing – review and editing.

DATA AVAILABILITY STATEMENT

With the exception of the i-Box data, both the raw and quality-controlled datasets used in this study can be found online. Specifically, the FDLR data can be retrieved from Adler *et al.* (2021a), the data from KITcube instruments can be found under Adler *et al.* (2021b), the Windcube data is provided under Adler *et al.* (2021c), and the SL88 and SLXR142 data can be retrieved from Gohm *et al.* (2021).

ORCID

Nevio Babić  <https://orcid.org/0000-0002-7299-7060>
Bianca Adler  <https://orcid.org/0000-0002-0384-7456>
Alexander Gohm  <https://orcid.org/0000-0003-4505-585X>
Norbert Kalthoff  <https://orcid.org/0000-0002-3322-7557>
Maren Haid  <https://orcid.org/0000-0002-9997-4088>
Manuela Lehner  <https://orcid.org/0000-0001-9600-0547>
Mathias W. Rotach  <https://orcid.org/0000-0003-2283-309X>

REFERENCES

- Adler, B. and Kalthoff, N. (2014) Multi-scale transport processes observed in the boundary layer over a mountainous island. *Boundary-Layer Meteorology*, 153, 515–537. <https://doi.org/10.1007/s10546-014-9957-8>.
- Adler, B., Kalthoff, N. and Kiseleva, O. (2020) Detection of structures in the horizontal wind field over complex terrain using coplanar Doppler lidar scans. *Meteorologische Zeitschrift*, 29, 467–481. <https://doi.org/10.1127/metz/2020/1031>.
- Adler, B., Babić, N., Kalthoff, N., Corsmeier, U., Kottmeier, C. and Mallaun, C. (2021a) CROSSINN (Cross-valley flow in the Inn Valley investigated by dual-Doppler lidar measurements) – Aircraft data set [FDLR]. Dataset on KITopen. Available at: <https://doi.org/10.5445/IR/1000127862>.
- Adler, B., Babić, N., Kalthoff, N. and Wieser, A. (2021b) CROSSINN (Cross-valley flow in the Inn Valley investigated by dual-Doppler lidar measurements) – KITcube data sets [CHM 15k, GRAW, HATPRO2, Mobotix, Photos]. Dataset on KITopen. Available at: <https://doi.org/10.5445/IR/1000127577>.
- Adler, B., Babić, N., Kalthoff, N. and Wieser, A. (2021c) CROSSINN (Cross-valley flow in the Inn Valley investigated by dual-Doppler lidar measurements) – KITcube data sets [WLS200s]. Dataset on KITopen. Available at: <https://doi.org/10.5445/IR/1000127847>.

- Adler, B., Gohm, A., Kalthoff, N., Babić, N., Corsmeier, U., Lehner, M., Rotach, M.W., Haid, M., Markmann, P., Gast, E., Tsaknakis, G. and Georgoussis, G. (2021d) CROSSINN – A field experiment to study the three-dimensional flow structure in the Inn Valley, Austria. *Bulletin of the American Meteorological Society*, 102, E38–E60. <https://doi.org/10.1175/BAMS-D-19-0283.1>.
- Azpiroz-Zabala, M., Cartigny, M.J.B., Sumner, E.J., Clare, M.A., Talling, P.J., Parsons, D.R. and Cooper, C. (2017) A general model for the helical structure of geophysical flows in channel bends. *Geophysical Research Letters*, 44, 11932–11941. <https://doi.org/10.1002/2017GL075721>.
- Banta, R.M., Shun, C., Law, D.C., Brown, W., Reinking, R.F., Hardesty, R.M., Senff, C.J., Brewer, W.A., Post, M. and Darby, L.S. (2013) Observational techniques: sampling the mountain atmosphere, pp. 409–530 in *Mountain Weather Research and Forecasting*, Chow, F.K., De Wekker, S.F.J., Snyder, B.J. (eds). Dordrecht, Netherlands: Springer.
- Becherer, J., Stacey, M.T., Umlauf, L. and Burchard, H. (2015) Lateral circulation generates flood tide stratification and estuarine exchange flow in a curved tidal inlet. *Journal of Physical Oceanography*, 45, 638–656. <https://doi.org/10.1175/JPO-D-14-0001.1>.
- Bingöl, F., Mann, J. and Foussekis, D. (2009) Conically scanning lidar error in complex terrain. *Meteorologische Zeitschrift*, 18, 189–195. <https://doi.org/10.1127/0941-2948/2009/0368>.
- Brehm, M. and Freytag, C. (1982) Erosion of the night-time thermal circulation in an Alpine valley. *Archives for Meteorology, Geophysics, and Bioclimatology, Series B*, 31, 331–352. <https://doi.org/10.1007/BF02263439>.
- Browning, K.A. and Wexler, R. (1968) The determination of kinematic properties of a wind field using Doppler radar. *Journal of Applied Meteorology*, 7, 105–113. [https://doi.org/10.1175/1520-0450\(1968\)007<0105:TDOKPO>2.0.CO;2](https://doi.org/10.1175/1520-0450(1968)007<0105:TDOKPO>2.0.CO;2).
- Calhoun, R., Heap, R., Princevac, M., Newsom, R., Fernando, H. and Ligon, D. (2006) Virtual towers using coherent Doppler lidar during the Joint Urban 2003 dispersion experiment. *Journal of Applied Meteorology and Climatology*, 45, 1116–1126. <https://doi.org/10.1175/JAM2391.1>.
- Chen, Q., Zhong, Q., Qi, M. and Wang, X. (2015) Comparison of vortex identification criteria for planar velocity fields in wall turbulence. *Physics of Fluids*, 27(8). <https://doi.org/10.1063/1.4927647>.
- Cherukuru, N.W., Calhoun, R., Lehner, M., Hoch, S.W. and Whiteman, C.D. (2015) Instrument configuration for dual-Doppler lidar coplanar scans: METCRAX II. *Journal of Applied Remote Sensing*, 9(1). <https://doi.org/10.1117/1.JRS.9.096090>.
- Corney, R.K., Peakall, J., Parsons, D.R., Elliott, L., Amos, K.J., Best, J.L., Keevil, G.M. and Ingham, D.B. (2006) The orientation of helical flow in curved channels. *Sedimentology*, 53, 249–257. <https://doi.org/10.1111/j.1365-3091.2006.00771.x>.
- Corney, R.K., Peakall, J., Parsons, D.R., Elliott, L., Best, J.L., Thomas, R.E., Keevil, G.M., Ingham, D.B. and Amos, K.J. (2008) Reply to Discussion of Imran et al. on “The orientation of helical flow in curved channels” by Corney et al., *Sedimentology*, 53, 249–257. *Sedimentology*, 55, 241–247. <https://doi.org/10.1111/j.1365-3091.2007.00925.x>.
- Cuxart, J. (2015) When can a high-resolution simulation over complex terrain be called LES? *Frontiers in Earth Science*, 3(87). <https://doi.org/10.3389/feart.2015.00087>.
- Davies-Jones, R.P. (1979) Dual-Doppler radar coverage area as a function of measurement accuracy and spatial resolution. *Journal of Applied Meteorology*, 18, 1229–1233. <https://doi.org/10.1175/1520-0450-18.9.1229>.
- De Wekker, S.F., Kossmann, M., Knierel, J.C., Giovannini, L., Gutmann, E.D. and Zardi, D. (2018) Meteorological applications benefiting from an improved understanding of atmospheric exchange processes over mountains. *Atmosphere*, 9(10). <https://doi.org/10.3390/atmos9100371>.
- Doyle, J.D., Grubišić, V., Brown, W.O., De Wekker, S.F., Dörnbrack, A., Jiang, Q., Mayor, S.D. and Weissmann, M. (2009) Observations and numerical simulations of subrotor vortices during T-REX. *Journal of the Atmospheric Sciences*, 66, 1229–1249. <https://doi.org/10.1175/2008JAS2933.1>.
- Dreiseitl, E. (1988) Slope and free air temperature in the Inn Valley. *Meteorology and Atmospheric Physics*, 39, 25–41. <https://doi.org/10.1007/BF01029895>.
- Emeis, S., Kalthoff, N., Adler, B., Pardyjak, E., Paci, A. and Junkermann, W. (2018) High-resolution observations of transport and exchange processes in mountainous terrain. *Atmosphere*, 9, 457. <https://doi.org/10.3390/atmos9120457>.
- Fernando, H., Mann, J., Palma, J., Lundquist, J.K., Barthelmie, R.J., Belo-Pereira, M., Brown, W., Chow, F., Gerz, T., Hocut, C., Klein, P.M., Leo, L.S., Matos, J.C., Oncley, S.P., Pryor, S.C., Bariteau, L., Bell, T.M., Bodini, N., Carney, M.B., Courtney, M.S., Creggan, E.D., Dimitrova, R., Gomes, S., Hagen, M., Hyde, J.O., Kigle, S., Krishnamurthy, R., Lopes, J.C., Mazzaro, L., Neher, J.M.T., Menke, R., Murphy, P., Oswald, L., Otarola-Bustos, S., Pattantyus, A.K., Veiga Rodrigues, C., Schady, A., Sirin, N., Spuler, S., Svensson, E., Tomaszewski, J., Turner, D.D., van Veen, L., Vasiljevic, N., Vassallo, D., Voss, S., Wildmann, N. and Wang, Y. (2019) The Perdigao: peering into microscale details of mountain winds. *Bulletin of the American Meteorological Society*, 100, 799–819. <https://doi.org/10.1175/BAMS-D-17-0227.1>.
- Freytag, C. (1987) Results from the MERKUR experiment: mass budget and vertical motions in a large valley during mountain and valley wind. *Meteorology and Atmospheric Physics*, 37, 129–140. <https://doi.org/10.1007/BF01040843>.
- Geyer, W.R. and MacCready, P. (2014) The estuarine circulation. *Annual Review of Fluid Mechanics*, 46, 175–197. <https://doi.org/10.1146/annurev-fluid-010313-141302>.
- Giorgio Serchi, F., Peakall, J., Ingham, D.B. and Burns, A.D. (2011) A unifying computational fluid dynamics investigation on the river-like to river-reversed secondary circulation in submarine channel bends. *Journal of Geophysical Research; Oceans*, 116(C6). <https://doi.org/10.1029/2010JC006361>.
- Giovannini, L., Ferrero, E., Karl, T., Rotach, M.W., Staquet, C., Trini Castelli, S. and Zardi, D. (2020) Atmospheric pollutant dispersion over complex terrain: challenges and needs for improving air quality measurements and modeling. *Atmosphere*, 11(6). <https://doi.org/10.3390/atmos11060646>.
- Goger, B., Rotach, M.W., Gohm, A., Fuhrer, O., Stiperski, I. and Holtzlag, A.A. (2018) The impact of three-dimensional effects on the simulation of turbulence kinetic energy in a major Alpine valley. *Boundary-Layer Meteorology*, 168, 1–27. <https://doi.org/10.1007/s10546-018-0341-y>.
- Goger, B., Rotach, M.W., Gohm, A., Stiperski, I., Fuhrer, O. and De Morsier, G. (2019) A new horizontal length-scale for a three-dimensional turbulence parameterization in mesoscale atmospheric modeling over highly complex terrain. *Journal of*

- Applied Meteorology and Climatology*, 58, 2087–2102. <https://doi.org/10.1175/JAMC-D-18-0328.1>.
- Gohm, A., Harnisch, F., Vergeiner, J., Obleitner, F., Schnitzhofer, R., Hansel, A., Fix, A., Neininger, B., Emeis, S. and Schäfer, K. (2009) Air pollution transport in an Alpine valley: results from airborne and ground-based observations. *Boundary-Layer Meteorology*, 131, 441–463. <https://doi.org/10.1007/s10546-009-9371-9>.
- Gohm, A., Mayr, G.J., Darby, L.S. and Banta, R.M. (2010) Evolution and structure of a cold front in an Alpine valley as revealed by a Doppler lidar. *Quarterly Journal of the Royal Meteorological Society*, 136, 962–977. <https://doi.org/10.1002/qj.609>.
- Gohm, A., Haid, M. and Rotach, M.W. (2021) CROSSINN (Cross-valley flow in the Inn Valley investigated by dual-Doppler lidar measurements) – ACINN Doppler wind lidar datasets (SL88, SLXR142). <https://doi.org/10.5281/zenodo.4585577>. Dataset on Zenodo.
- Grubišić, V., Doyle, J.D., Kuettner, J., Mobbs, S., Smith, R.B., Whiteman, C.D., Dirks, R., Czyzyk, S., Cohn, S.A., Vosper, S.B., Weissmann, M., Haimov, S., De Wekker, S.F.J., Pan, L.L. and Chow, F.K. (2008) The terrain-induced rotor experiment: a field campaign overview including observational highlights. *Bulletin of the American Meteorological Society*, 89, 1513–1534. <https://doi.org/10.1175/2008BAMS2487.1>.
- Haid, M. (2019) marenha/doppler_wind_lidar_toolbox: first release (v1.0.0). <https://doi.org/10.5281/zenodo.3583083>. Dataset on Zenodo.
- Haid, M., Gohm, A., Umek, L., Ward, H., Muschinski, T., Lehner, L. and Rotach, M.W. (2020) Foehn–cold pool interactions in the Inn Valley during PIANO IOP2. *Quarterly Journal of the Royal Meteorological Society*, 146, 1232–1263. <https://doi.org/10.1002/qj.3735>.
- Harnisch, F., Gohm, A., Fix, A., Schnitzhofer, R., Hansel, A. and Neininger, B. (2009) Spatial distribution of aerosols in the Inn Valley atmosphere during wintertime. *Meteorology and Atmospheric Physics*, 103, 223–235. <https://doi.org/10.1007/s00703-008-0318-3>.
- Hersbach, H., Bell, B., Berrisford, P., Hirahara, S., Horányi, A., Muñoz-Sabater, J., Nicolas, J., Peubey, C., Radu, R., Schepers, D., Simmons, A., Soci, C., Abdalla, S., Abellan, X., Balsamo, G., Bechtold, P., Biavati, G., Bidlot, J., Bonavita, M., De Chiara, G., Dahlgren, P., Dee, D.P., Diamantakis, M., Dragani, R., Flemming, J., Forbes, R., Fuentes, M., Geer, A., Haimberger, L., Healy, S., Hogan, R.J., Hólm, E.V., Janisková, M., Keeley, S., Laloyaux, P., Lopez, P., Lupu, C., Radnoti, G., de Rosnay, P., Rozum, I., Vamborg, F., Villaume, S. and Thépaut, J.-N. (2020) The ERA5 global reanalysis. *Quarterly Journal of the Royal Meteorological Society*, 146, 1999–2049. <https://doi.org/10.1002/qj.3803>.
- Hill, M., Calhoun, R., Fernando, H., Wieser, A., Dörnbrack, A., Weissmann, M., Mayr, G. and Newsom, R. (2010) Coplanar Doppler lidar retrieval of rotors from T-REX. *Journal of the Atmospheric Sciences*, 67, 713–729. <https://doi.org/10.1175/2009JAS3016.1>.
- Holton, J.R. (2004) *An Introduction to Dynamic Meteorology*. London, UK: Elsevier Academic.
- Jackson, P.L., Mayr, G. and Vosper, S.B. (2013) Dynamically-driven winds, pp. 121–218 in *Mountain Weather Research and Forecasting*. Chow, F.K., De Wekker, S.F.J., Snyder, B.J. (eds). Dordrecht, Netherlands: Springer.
- Janocko, M., Cartigny, M., Nemec, W. and Hansen, E. (2013) Turbidity current hydraulics and sediment deposition in erodible sinuous channels: laboratory experiments and numerical simulations. *Marine and Petroleum Geology*, 41, 222–249. <https://doi.org/10.1016/j.marpetgeo.2012.08.012>.
- Kalkwijk, J.P.T. and Booij, R. (1986) Adaptation of secondary flow in nearly-horizontal flow. *Journal of Hydraulic Research*, 24, 19–37. <https://doi.org/10.1080/00221688609499330>.
- Kalthoff, N., Adler, B., Wieser, A., Kohler, M., Träumner, K., Handwerker, J., Corsmeier, U., Khodayar, S., Lambert, D., Kopmann, A., Kunka, N., Dick, G., Ramatschi, M., Wickert, J. and Kottmeier, C. (2013) KITcube: a mobile observation platform for convection studies deployed during HyMeX. *Meteorologische Zeitschrift*, 22, 633–647. <https://doi.org/10.1127/0941-2948/2013/0542>.
- Karl, T., Gohm, A., Rotach, M.W., Ward, H.C., Graus, M., Cede, A., Wohlfahrt, G., Hammerle, A., Haid, M., Tiefengraber, M., Lamprecht, C., Vergeiner, J., Kreuter, A., Wagner, J. and Staudinger, M. (2020) Studying urban climate and air quality in the Alps: the Innsbruck atmospheric observatory. *Bulletin of the American Meteorological Society*, 101, E488–E507. <https://doi.org/10.1175/BAMS-D-19-0270.1>.
- Kim, Y.H. and Voulgaris, G. (2008) Lateral circulation and suspended sediment transport in a curved estuarine channel: Winyah Bay, SC, USA. *Journal of Geophysical Research; Oceans*, 113(C9). <https://doi.org/10.1029/2007JC004509>.
- Lacy, J.R. and Monismith, S.G. (2001) Secondary currents in a curved, stratified, estuarine channel. *Journal of Geophysical Research; Oceans*, 106, 31283–31302. <https://doi.org/10.1029/2000JC000606>.
- Ladstätter, P. (2020) Vertical structure of the atmospheric boundary layer in the Inn Valley during CROSSINN. Master's thesis, University of Innsbruck, Austria.
- Lehner, M. and Rotach, M.W. (2018) Current challenges in understanding and predicting transport and exchange in the atmosphere over mountainous terrain. *Atmosphere*, 9(7). <https://doi.org/10.3390/atmos9070276>.
- Lehner, M., Whiteman, C.D., Hoch, S.W., Crosman, E.T., Jeglum, M.E., Cherukuru, N.W., Calhoun, R., Adler, B., Kalthoff, N., Rotunno, R., Horst, T.W., Semmer, S., Brown, W.O.J., Oncley, S.P., Vogt, R., Grudzielanek, A.M., Cermak, J., Fonteyne, N.J., Bernhofer, C., Pitacco, A. and Klein, P. (2016) The METCRAX II field experiment: a study of downslope windstorm-type flows in Arizona's Meteor Crater. *Bulletin of the American Meteorological Society*, 97, 217–235. <https://doi.org/10.1175/BAMS-D-14-00238.1>.
- Lehner, M., Rotach, M.W. and Obleitner, F. (2019) A method to identify synoptically undisturbed, clear-sky conditions for valley-wind analysis. *Boundary-Layer Meteorology*, 173, 435–450. <https://doi.org/10.1007/s10546-019-00471-2>.
- Lehner, M., Rotach, M.W., Sfyri, E. and Obleitner, F. (2021) Spatial and temporal variations in near-surface energy fluxes in an Alpine valley under synoptically undisturbed and clear-sky conditions. *Quarterly Journal of the Royal Meteorological Society*, 147, 2173–2196. <https://doi.org/10.1002/qj.4016>.
- Mallaun, C., Giez, A. and Baumann, R. (2015) Calibration of 3-D wind measurements on a single-engine research aircraft. *Atmospheric Measurement Techniques*, 8, 3177–3196. <https://doi.org/10.5194/amt-8-3177-2015>.

- Massaro, G., Stiperski, I., Pospichal, B. and Rotach, M. (2015) Accuracy of retrieving temperature and humidity profiles by ground-based microwave radiometry in truly complex terrain. *Atmospheric Measurement Techniques*, 8, 3355–3367. <https://doi.org/10.5194/amt-8-3355-2015>.
- Newsom, R.K., Ligon, D., Calhoun, R., Heap, R., Cregan, E. and Princevac, M. (2005) Retrieval of microscale wind and temperature fields from single- and dual-Doppler lidar data. *Journal of Applied Meteorology*, 44, 1324–1345. <https://doi.org/10.1175/JAM2280.1>.
- Nickus, U. and Vergeiner, I. (1984) The thermal structure of the Inn Valley atmosphere. *Archives for Meteorology, Geophysics, and Bioclimatology, Series A*, 33, 199–215. <https://doi.org/10.1007/BF02257725>.
- Nidzieko, N.J., Hench, J.L. and Monismith, S.G. (2009) Lateral circulation in well-mixed and stratified estuarine flows with curvature. *Journal of Physical Oceanography*, 39, 831–851. <https://doi.org/10.1175/2008JPO4017.1>.
- Peakall, J. and Sumner, E.J. (2015) Submarine channel flow processes and deposits: a process-product perspective. *Geomorphology*, 244, 95–120. <https://doi.org/10.1016/j.geomorph.2015.03.005>.
- Raasch, S. and Harbusch, G. (2001) An analysis of secondary circulations and their effects caused by small-scale surface inhomogeneities using large-eddy simulation. *Boundary-Layer Meteorology*, 101, 31–59. <https://doi.org/10.1023/A:1019297504109>.
- Rotach, M.W., Wohlfahrt, G., Hansel, A., Reif, M., Wagner, J. and Gohm, A. (2014) The world is not flat: implications for the global carbon balance. *Bulletin of the American Meteorological Society*, 95, 1021–1028. <https://doi.org/10.1175/BAMS-D-13-00109.1>.
- Rotach, M.W., Gohm, A., Lang, M.N., Leukauf, D., Stiperski, I. and Wagner, J.S. (2015) On the vertical exchange of heat, mass, and momentum over complex, mountainous terrain. *Frontiers in Earth Science*, 3. <https://doi.org/10.3389/feart.2015.00076>.
- Rotach, M.W., Stiperski, I., Fuhrer, O., Goger, B., Gohm, A., Obleitner, F., Rau, G., Sfyri, E. and Vergeiner, J. (2017) Investigating exchange processes over complex topography: the Innsbruck Box (i-Box). *Bulletin of the American Meteorological Society*, 98, 787–805. <https://doi.org/10.1175/BAMS-D-15-00246.1>.
- Russell, P. and Vennell, R. (2014) Distribution of vertical velocity inferred from secondary flow in a curved tidal channel. *Journal of Geophysical Research; Oceans*, 119, 6010–6023. <https://doi.org/10.1002/2014JC010003>.
- Santos, P., Mann, J., Vasiljević, N., Cantero, E., Sanz Rodrigo, J., Borbón, F., Martínez-Villagrasa, D., Martí, B. and Cuxart, J. (2020) The Alaiz experiment: untangling multi-scale stratified flows over complex terrain. *Wind Energy Science*, 5, 1793–1810. <https://doi.org/10.5194/wes-5-1793-2020>.
- Serafin, S., Adler, B., Cuxart, J., De Wekker, S.F., Gohm, A., Grisono, B., Kalthoff, N., Kirshbaum, D.J., Rotach, M.W., Schmidli, J., Stiperski, I., Vecenaj, Z. and Zardi, D. (2018) Exchange processes in the atmospheric boundary layer over mountainous terrain. *Atmosphere*, 9(3). <https://doi.org/10.3390/atmos9030102>.
- Serafin, S., Rotach, M.W., Arpagaus, M., Colfescu, I., Cuxart, J., De Wekker, S.F., Ewans, M.J., Grubišić, V., Kalthoff, N., Karl, T., Kirshbaum, D.J., Lehner, M., Mobbs, S.D., Paci, A., Palazzi, E., Raudzens Bailey, A., Schmidli, J., Wohlfahrt, G. and Zardi, D. (2020) *Multi-scale Transport and Exchange Processes in the Atmosphere Over Mountains: Programme and Experiment*. Innsbruck, Austria: Innsbruck University Press. <https://doi.org/10.15203/99106-003-1>.
- Sfyri, E., Rotach, M.W., Stiperski, I., Bosveld, F.C., Lehner, M. and Obleitner, F. (2018) Scalar-flux similarity in the layer near the surface over mountainous terrain. *Boundary-Layer Meteorology*, 169, 11–46. <https://doi.org/10.1007/s10546-018-0365-3>.
- Stawarski, C., Träumner, K., Knigge, C. and Calhoun, R. (2013) Scopes and challenges of dual-Doppler lidar wind measurements – An error analysis. *Journal of Atmospheric and Oceanic Technology*, 30, 2044–2062. <https://doi.org/10.1175/JTECH-D-12-00244.1>.
- Stiperski, I., Calaf, M. and Rotach, M.W. (2019) Scaling, anisotropy, and complexity in near-surface atmospheric turbulence. *Journal of Geophysical Research; Atmospheres*, 124, 1428–1448. <https://doi.org/10.1029/2018JD029383>.
- Stiperski, I. and Rotach, M.W. (2016) On the measurement of turbulence over complex mountainous terrain. *Boundary-Layer Meteorology*, 159, 97–121. <https://doi.org/10.1007/s10546-015-0103-z>.
- Stith, J.L., Baumgardner, D., Haggerty, J., Hardesty, R.M., Lee, W.-C., Lenschow, D., Pilewskie, P., Smith, P.L., Steiner, M. and Vömel, H. (2018) 100 years of progress in atmospheric observing systems. *Meteorological Monographs*, 59, 2.1–2.55. <https://doi.org/10.1175/AMSMONOGRAPH-D-18-0006.1>.
- Stull, R.B. (1988) *An Introduction to Boundary Layer Meteorology*. Dordrecht, Netherlands: Kluwer Academic.
- Umek, L., Gohm, A., Haid, M., Ward, H.C. and Rotach, M.W. (2020) Large-eddy simulation of foehn-cold pool interactions in the Inn Valley during PIANO IOP 2. *Quarterly Journal of the Royal Meteorological Society*, 147, 944–982. <https://doi.org/10.1002/qj.3954>.
- Van Heerwaarden, C.C., Mellado, J.P. and De Lozar, A. (2014) Scaling laws for the heterogeneously heated free convective boundary layer. *Journal of the Atmospheric Sciences*, 71, 3975–4000. <https://doi.org/10.1175/JAS-D-13-0383.1>.
- Vergeiner, I. and Dreiseitl, E. (1987) Valley winds and slope winds – Observations and elementary thoughts. *Meteorology and Atmospheric Physics*, 36, 264–286. <https://doi.org/10.1007/BF01045154>.
- Vosper, S.B., Ross, A.N., Renfrew, I.A., Sheridan, P.F., Elvidge, A.D. and Grubišić, V. (2018) Current challenges in orographic flow dynamics: turbulent exchange due to low-level gravity-wave processes. *Atmosphere*, 9(9). <https://doi.org/10.3390/atmos9090361>.
- Weigel, A.P. and Rotach, M.W. (2004) Flow structure and turbulence characteristics of the daytime atmosphere in a steep and narrow Alpine valley. *Quarterly Journal of the Royal Meteorological Society*, 130, 2605–2627. <https://doi.org/10.1256/qj.03.214>.
- Weigel, A.P., Chow, F.K., Rotach, M.W., Street, R.L. and Xue, M. (2006) High-resolution large-eddy simulations of flow in a steep Alpine valley. Part II: flow structure and heat budgets. *Journal of Applied Meteorology and Climatology*, 45, 87–107. <https://doi.org/10.1175/JAM2323.1>.
- Whiteman, C.D. (2000) *Mountain Meteorology: Fundamentals and Applications*. Oxford, UK: Oxford University Press.
- Whiteman, C.D. and Hoch, S.W. (2014) Pseudovertical temperature profiles in a broad valley from lines of temperature sensors on sidewalls. *Journal of Applied Meteorology and Climatology*, 53, 2430–2437. <https://doi.org/10.1175/JAMC-D-14-0177.1>.
- Whiteman, C.D., Lehner, M., Hoch, S.W., Adler, B., Kalthoff, N. and Haiden, T. (2018a) Katabatically driven cold air intrusions into a

- basin atmosphere. *Journal of Applied Meteorology and Climatology*, 57, 435–455. <https://doi.org/10.1175/JAMC-D-17-0131.1>.
- Whiteman, C.D., Lehner, M., Hoch, S.W., Adler, B., Kalthoff, N., Vogt, R., Feigenwinter, I., Haiden, T. and Hills, M.O. (2018b) The nocturnal evolution of atmospheric structure in a basin as a larger-scale katabatic flow is lifted over its rim. *Journal of Applied Meteorology and Climatology*, 57, 969–989. <https://doi.org/10.1175/JAMC-D-17-0156.1>.
- Wildmann, N., Kigle, S. and Gerz, T. (2018) Coplanar lidar measurement of a single wind energy converter wake in distinct atmospheric stability regimes at the Perdigão 2017 experiment. *Journal of Physics: Conference Series*, 1037(5). <https://doi.org/10.1088/1742-6596/1037/5/052006>.
- Zängl, G. (2004) A reexamination of the valley wind system in the Alpine Inn Valley with numerical simulations. *Meteorology and Atmospheric Physics*, 87, 241–256. <https://doi.org/10.1007/s00703-003-0056-5>.
- Zängl, G. (2009) The impact of weak synoptic forcing on the valley-wind circulation in the Alpine Inn Valley. *Meteorology and Atmospheric Physics*, 105, 37–53. <https://doi.org/10.1007/s00703-009-0030-y>.
- Zardi, D. and Whiteman, C.D. (2013) Diurnal mountain wind systems, pp. 35–119 in *Mountain Weather Research and Forecasting* Chow, F.K., De Wekker, S.F.J., Snyder, B.J. (eds). Dordrecht, Netherlands: Springer.

SUPPORTING INFORMATION

Additional supporting information may be found online in the Supporting Information section at the end of this article.

How to cite this article: Babić, N., Adler, B., Gohm, A., Kalthoff, N., Haid, M., Lehner, M. *et al.* (2021) Cross-valley vortices in the Inn valley, Austria: Structure, evolution and governing force imbalances. *Quarterly Journal of the Royal Meteorological Society*, 147(740), 3835–3861. Available from: <https://doi.org/10.1002/qj.4159>